

# Semi-analytical calculation of the trajectory of relativistic nuclear collisions in the QCD phase diagram

Todd Mendenhall\* and Zi-Wei Lin†

*Department of Physics, East Carolina University, Greenville, NC 27858*

(Dated: March 17, 2023)

We extend a semi-analytical model that includes the finite nuclear thickness to calculate the energy density  $\epsilon(t)$  and conserved-charge densities including the net-baryon density  $n_B(t)$  produced at mid-spacetime-rapidity in central Au+Au collisions. Assuming the formation of a quark-gluon plasma with an ideal gas equation of state of either quantum or Boltzmann statistics or with a lattice QCD-based equation of state, we extract the temperature  $T$  and chemical potentials  $\mu_B$ ,  $\mu_Q$  and  $\mu_S$  as functions of time. This then allows us to semi-analytically calculate the  $T - \mu_B$  trajectory of relativistic nuclear collisions in the QCD phase diagram, which should benefit the studies of high density physics including the search for the critical end point. This model is also useful for exploring the trajectories in the more general  $T - \mu_B - \mu_Q - \mu_S$  QCD phase space.

## I. INTRODUCTION

Experiments at the Relativistic Heavy Ion Collider (RHIC) at BNL [1] and the Large Hadron Collider (LHC) at CERN [2] have produced the Quark-Gluon Plasma (QGP) with ultrarelativistic nuclear collisions. The QGP is an exotic phase of matter in which the temperature and density are high enough to “melt” hadrons [3]. Such a system of unbound quarks and gluons can only exist for a short time before the partons recombine into hadrons due to confinement. The fleeting nature of the QGP makes studying its properties very difficult, but the success in this endeavor would expand our understanding of the earliest stage of the universe during which the QGP is believed to have existed. Learning about the QGP properties would also enable the testing of Quantum Chromodynamics (QCD) as the fundamental theory governing the strong interaction [4]. Of particular interest to the field is understanding the phase transition from hadronic to partonic matter in the QCD phase diagram [5]. Lattice QCD results show that it is a smooth crossover at zero baryon chemical potential  $\mu_B$  [6], but calculations at finite  $\mu_B$  are difficult [7].

The conjectured critical end point (CEP) of the first-order phase transition line is of special interest [8]. The Beam Energy Scan (BES) program at RHIC uses Au+Au collisions at a variety of energies to search for the CEP [9–11]. The matter created in a given collision system, for example, at a given collision energy and centrality (or impact parameter), follows a unique average trajectory and freezes out at a unique point on average in the QCD phase diagram. Here, “average” refers to averaging over many events of the given collision system. The time evolutions of the temperature  $T$  and baryon chemical potential  $\mu_B$  together determine the system’s history in the QCD phase diagram. For those collisions where the tra-

jectory is near the CEP, event-by-event fluctuations in conserved quantities could point to the existence of the CEP [12]. For example, event-by-event net-proton cumulant ratios at low collision energies could prove useful for locating the CEP [13].

Since the matter in ultrarelativistic nuclear collisions progresses through several stages, it is not straightforward to correlate experimental measurements with the QGP thermodynamic properties. Dynamical models including hydrodynamic models and transport models [14–17] have been used to study the evolution of the thermodynamic properties of the QCD matter created during high energy nuclear collisions. Additionally, semi-analytical models of the initial energy density production [18–20] have progressively expanded our understanding of the early time evolution of the energy densities produced in such collisions. In particular, it has been shown that the effect of the finite nuclear thickness drastically alters the peak energy density  $\epsilon^{\max}$  at low collision energies such as the BES energies [19, 20].

The purpose of this study is to calculate trajectories in the QCD phase diagram of the matter produced in central Au+Au collisions for collision energies  $\sqrt{s_{NN}}$  up to 200 GeV. Note that all of our results here are for the central spacetime rapidity region ( $\eta_s = 0$ ), where our semi-analytical model [20] has been defined. The paper is organized into the following sections after the Introduction. First, we describe our semi-analytical model [20] for calculating the energy density  $\epsilon(t)$  and conserved-charge densities in Sec. II A. Second, we discuss the thermodynamic equations governing an ideal gas of massless gluons and quarks under quantum (Bose-Einstein and Fermi-Dirac) statistics in Sec. II B and Boltzmann statistics in Sec. II C. For the remainder of this paper, we will refer to the ideal gas equation of state (EoS) with quantum statistics as the quantum EoS and the ideal gas EoS with Boltzmann statistics as the Boltzmann EoS. For completeness, the general relations between  $\epsilon$ ,  $n$  and  $T$ ,  $\mu$  that lead to the thermodynamic equations of our semi-analytical model are provided in the Appendix for both the quantum EoS and the Boltzmann EoS. Third, we in-

\*Electronic address: [mendenhallt16@students.ecu.edu](mailto:mendenhallt16@students.ecu.edu)

†Electronic address: [linz@ecu.edu](mailto:linz@ecu.edu)

roduce in Sec. IID a lattice QCD-based EoS, which we will refer to as the lattice EoS, that provides a more realistic relationship between  $\epsilon$ ,  $n$  and  $T$ ,  $\mu$  (at least at small  $\mu_B$ ). We then present our results for  $\epsilon(t)$  and  $n_B(t)$  in Sec. IIIA, and give our results for the extracted  $T(t)$ ,  $\mu_B(t)$ ,  $\mu_Q(t)$ ,  $\mu_S(t)$  and the resultant  $T - \mu_B$  trajectories for the quantum EoS in Sec. IIIB and the Boltzmann EoS in Sec. IIIC. In Sec. IIID, we show the results for the extracted trajectories by applying the lattice EoS to the densities calculated from our semi-analytical model. We then consider the effect of transverse expansion on the trajectories in Sec. IIIE. Results for the QGP lifetime for all three equations of state are presented in Sec. IIIF. We then discuss the improved net-baryon rapidity density parameterization, the effect of a finite  $s$ -quark mass, the near-zero value of the calculated  $\mu_Q$ , and the implications of strangeness neutrality on the results using the lattice EoS in Sec. IV. Finally, we conclude in Sec. V.

## II. METHODS

### A. Calculating energy and net conserved-charge densities

Naively, one can use the method of the Bjorken energy density formula [18], in which partons at mid-rapidity are produced at  $t = 0$  and  $z = 0$ , to predict the time evolution of the initial energy density  $\epsilon(t)$ :

$$\epsilon^{Bj}(t) = \frac{1}{A_T} \frac{dE_T}{t dy}. \quad (1)$$

Here,  $A_T = \pi R_A^2$  is the full transverse overlap area of two nuclei in central A+A collisions, and  $dE_T/dy$  is the transverse energy per rapidity at mid-rapidity. Because Eq.(1) predicts a diverging  $\epsilon$  as  $t \rightarrow 0$ , one must choose a finite initial time  $\tau_F$ , which can be considered as the time when partons are formed. For high collision energies, such as the top RHIC energy of  $\sqrt{s_{NN}} = 200$  GeV, the finite thickness of the Lorentz-contracted nucleus is small compared to the typical  $\tau_F$  value, so Bjorken's formula is valid. However, for lower collision energies where the crossing time  $d_t = 2R_A/\sinh y_{CM}$  is comparable to or even greater than  $\tau_F$ , Eq.(1) is expected to break down [21]. Note that  $y_{CM}$  is the rapidity of the projectile nucleus in the center-of-mass frame, and we use  $R_A = 1.12A^{1/3}$  fm for the hard-sphere nuclear radius. Also note that the transverse expansion of the overlap volume is neglected until Sec. IIIE. Furthermore, the slowing down of participant nucleons, and secondary parton or hadron scatterings are neglected in our semi-analytical study, as done in previous similar studies [18–20].

We have shown earlier [19, 20] that the finite nuclear thickness must be considered when estimating  $\epsilon(t)$  at low collision energies. Therefore, a more realistic model of the initial energy production is one in which partons are

produced within a finite range of time and longitudinal position [20]. This improved model has been shown to predict a finite  $\epsilon^{\max}$  for  $\tau_F = 0$  fm/c, while earlier models [18, 19] predict infinite  $\epsilon^{\max}$  there. In this model [20], the initial energy density at time  $t$  averaged over the full transverse overlap area is given by

$$\epsilon(t) = \frac{1}{A_T} \iint_S \frac{dx dz_0}{t-x} \frac{d^3 m_T}{dx dz_0 dy} \cosh^3 y. \quad (2)$$

In the above,  $S$  represents the production area in the initial production time  $x$  and longitudinal position  $z_0$  at observation time  $t$ . The production area  $S$  is the portion of the overlap region  $S_0$  below the formation time hyperbola of Eq. (11). This ensures that a parton will contribute to the energy or net-charge density at time  $t$  after its formation time has passed. The overlap region  $S_0$  is a diamond along the vertical ( $t$ ) axis with one vertex at  $(0, 0)$  and the other at  $(0, d_t)$  in the  $t-z$  plane. The width of the overlap region corresponds to the thickness in the  $z$ -direction of the overlapping Lorentz-contracted spherical nuclei. Therefore, the width  $\Delta z$  at  $t = 0$  and  $t = d_t$  are both zero, since these are the times when the nuclei would just touch or completely pass through each other. At  $t = d_t/2$ , the width is maximal at  $\Delta z = 2R_A/\gamma$ . One key difference between our picture and that of the Bjorken energy density formula is that the overlapping and expanding stages cannot be clearly separated but are instead mixed together. We assume that partons free-stream from their production point  $(z_0, x)$  during time  $t \in (x, x + \tau_F \cosh y)$  and could then interact with the medium after its formation time. In our model, the velocity along the  $z$ -direction of a produced parton is  $v_z = (z - z_0)/(t - x)$ , while in the Bjorken picture  $v_z = z/t$  because all partons are produced at  $(z_0, x) = (0, 0)$ . On the other hand, our model is similar to the Bjorken energy density formula in that all secondary interactions are ignored.

To be general, the initial energy is assumed to be produced within  $x \in [t_1, t_2]$  (instead of the naive range  $[0, d_t]$ ). The resulting  $\epsilon(t)$  is a piecewise function of  $t$ , where the pieces are determined by the integration limits in Eq.(2) and are listed in Table I (see Ref. [20] for details). Note that  $\epsilon(t) = 0$  for  $t \in [0, t_1 + \tau_F]$ .

In this study, we assume that  $d^3 m_T/(dx dz_0 dy)$  in Eq.(2) is factorized:

$$\frac{d^3 m_T}{dx dz_0 dy} = g(z_0, x) \frac{dm_T}{dy}. \quad (3)$$

The weighting function  $g(z_0, x)$  is normalized as  $\iint_{S_0} g(z_0, x) dx dz_0 = 1$ , where  $S_0$  is the area of the entire diamond-shaped production region in the  $t-z$  plane [20]. This normalization condition ensures that  $dm_T/dy$  represents the initial transverse mass rapidity density of all produced partons. We further make the simplest assumption that partons are produced uniformly throughout  $S_0$ , which leads to  $g(z_0, x) = 2/(\beta t_{21}^2)$ , where  $\beta = \tanh y_{CM}$  and  $t_{21} = t_2 - t_1$ . Next, we take the following specific

Piece	$t$ -range	$x$ -range	$z_0$ -range
$\epsilon_I(t)$ or $n_{B,I}(t)$	$[t_1 + \tau_F, t_a)$	$[t_1, x_1)$ $[x_1, t - \tau_F]$	$[-\beta(x - t_1), \beta(x - t_1)]$ $[-z_F(x), z_F(x)]$
$\epsilon_{II}(t)$ or $n_{B,II}(t)$	$[t_a, t_2 + \tau_F)$	$[t_1, t_{\text{mid}})$ $[t_{\text{mid}}, x_2)$ $[x_2, t - \tau_F]$	$[-\beta(x - t_1), \beta(x - t_1)]$ $[-\beta(t_2 - x), \beta(t_2 - x)]$ $[-z_F(x), z_F(x)]$
$\epsilon_{III}(t)$ or $n_{B,III}(t)$	$[t_2 + \tau_F, \infty)$	$[t_1, t_{\text{mid}})$ $[t_{\text{mid}}, x_2]$	$[-\beta(x - t_1), \beta(x - t_1)]$ $[-\beta(t_2 - x), \beta(t_2 - x)]$

TABLE I: Piecewise solution of  $\epsilon(t)$  and  $n_B(t)$  as functions of the observation time  $t$ , where the integration limits for each piece are written in the format  $x \in [x^{\min}, x^{\max}]$  and  $z_0 \in [z_0^{\min}, z_0^{\max}]$  for each part of the production area in the initial production time  $x$  and longitudinal position  $z_0$  [20].

form for  $dm_T/dy$  [20]:

$$\frac{dm_T}{dy} = \frac{dE_T}{dy} + m_N \frac{dN_{\text{netB}}}{dy}, \quad (4)$$

where  $m_N$  is the nucleon mass. We assume that the  $dE_T/dy$  term is described by a single Gaussian function while  $dN_{\text{netB}}/dy$  is described by a double Gaussian [20]:

$$\frac{dE_T}{dy} = \frac{dE_T}{dy}(0) \exp\left(-\frac{y^2}{2\sigma_1^2}\right), \quad (5)$$

$$\frac{dN_{\text{netB}}}{dy} \propto \exp\left[-\frac{(y + y_B)^2}{2\sigma_2^2}\right] + \exp\left[-\frac{(y - y_B)^2}{2\sigma_2^2}\right]. \quad (6)$$

The transverse energy rapidity density at mid-rapidity is parameterized as  $dE_T/dy(0) = 1.25 dE_T/d\eta(0)$ , where  $dE_T/d\eta(0)$  at  $\sqrt{s_{\text{NN}}} > 20.7$  GeV is taken as the parameterization given by the PHENIX Collaboration [22], while  $dE_T/d\eta(0)$  at lower energies is given by an improved parameterization [20]. We use the following parameterizations for the Gaussian parameters  $y_B$  and  $\sigma_2$ :

$$y_B = 0.599 \left[ 1 - \frac{1}{2.18 + \ln^{1.86}\left(\frac{\sqrt{s_{\text{NN}}}}{E_0}\right)} \right] y_{\text{CM}},$$

$$\sigma_2 = 0.838 \left[ 1 - \frac{1}{5.01 + \ln^{1.61}\left(\frac{\sqrt{s_{\text{NN}}}}{E_0}\right)} \right] \sqrt{\ln\left(\frac{\sqrt{s_{\text{NN}}}}{E_0}\right)} \quad (7)$$

with  $E_0 = 2m_N$  being the threshold energy. Note that these parameterizations are different from those used in our earlier study [20], and we explain our reasoning in Sec. IV. These parameterizations have been obtained using the proton  $dN/dy$  data at  $\sqrt{s_{\text{NN}}} = 2.65, 3.30, 3.85,$  and  $4.31$  GeV [23] and the net-proton  $dN/dy$  data at  $\sqrt{s_{\text{NN}}} = 4.87$  [24, 25],  $8.77$  [26],  $17.3$  [27],  $62.4$  [28] and  $200$  GeV [29] in central Au+Au collisions (with the exception that central Pb+Pb data are used at  $8.8$  and

$17.3$  GeV). The value of the proportionality constant in Eq.(6) is determined from the conservation of total net-baryon number  $\int (dN_{\text{netB}}/dy) dy = 2A$  at each collision energy. Finally, the Gaussian parameter  $\sigma_1$  in Eq.(5) is calculated using the conservation of total energy  $\int (dm_T/dy) \cosh y dy = A\sqrt{s_{\text{NN}}}$  at each collision energy.

In our semi-analytical model [19, 20], the primary collisions between the two nuclei start at time  $t_1$  and end at time  $t_2$ . In this study, we take

$$t_1 = \frac{1}{6}d_t, \quad t_2 = \frac{5}{6}d_t, \quad (8)$$

because this choice gives  $\epsilon^{\max} = 2\rho_0 m_N$  and  $n_B^{\max} = 2\rho_0$  for the threshold collision energy  $\sqrt{s_{\text{NN}}} = E_0$ , which would be expected if the two nuclei would just fully overlap. Note that  $\rho_0 \approx 0.17 \text{ fm}^{-3}$  in the hard sphere model for the nucleus. Also note that in previous studies [19, 20],  $t_1 = 0.2d_t$  and  $t_2 = 0.8d_t$  were used so that the width of the production time distribution was similar to the results from the string melting version of a multi-phase transport (AMPT) model [30]. In Table I, time  $t_a$  is given by

$$t_a = t_{\text{mid}} + \sqrt{\tau_F^2 + \left(\frac{\beta t_{21}}{2}\right)^2} \quad (9)$$

with  $t_{\text{mid}} = (t_1 + t_2)/2$ , times  $x_1$  and  $x_2$  are given by

$$x_i = \frac{t - \beta^2 t_i - \sqrt{\beta^2[(t - t_i)^2 - \tau_F^2] + \tau_F^2}}{1 - \beta^2} \quad (10)$$

for  $i = 1$  or  $2$ , and the function  $z_F(x)$  is given by

$$z_F(x) = \sqrt{(t - x)^2 - \tau_F^2}. \quad (11)$$

We now calculate the net-baryon density  $n_B(t)$  using the same method as that used for the  $\epsilon(t)$  calculation [20].

We then obtain the following equation for the net-baryon density that is similar to Eq.(2):

$$n_B(t) = \frac{1}{A_T} \iint_S \frac{dx dz_0}{t-x} \frac{d^3 N_{\text{netB}}}{dx dz_0 dy} \cosh^2 y. \quad (12)$$

Note that there is one less power of  $\cosh y$  in this equation than in Eq.(2) because that equation involves  $E = m_T \cosh y$ . We also assume the same factorization  $d^3 N_{\text{netB}}/(dx dz_0 dy) = 2/(\beta t_{21}^2) dN_{\text{netB}}/dy$ . Therefore, the net-baryon density  $n_B(t)$  is also given by a piecewise solution, as shown in Table I.

Since the net-electric charge is carried by the incoming protons while the net-baryon number is carried by the incoming nucleons in the nuclei, we assume that the initial production from the primary NN collisions is independent of whether N is a proton or a neutron. Our semi-analytical method then leads to

$$n_Q(t) = n_B(t) \frac{Z}{A}, \quad (13)$$

where  $Z$  and  $A$  represent the atomic number and mass number of the nucleus, respectively, in the symmetric A+A system. Note that the relationship  $n_Q/n_B = Z/A$  has also been used in other studies [31]. Furthermore, since the incoming nuclei do not carry net-strangeness, we assume that the initial production is symmetric for  $s$  and  $\bar{s}$ . For the net-strangeness density, our semi-analytical method then simply gives

$$n_s(t) = 0, \quad (14)$$

i.e., strangeness neutrality.

### B. Thermodynamics of a massless QGP with the quantum EoS

According to Eq.(A.8) or Eq.(A.12), the result  $n_s = 0$  from our semi-analytical model gives the following relation

$$\mu_B - \mu_Q - 3\mu_s = 0 \quad (15)$$

for the ideal gas equation of state with either quantum or Boltzmann statistics, which corresponds to  $\mu_s = 0$  for the strange quark chemical potential. Using this relation, the general results in Eqs.(A.5)-(A.7) for quantum statistics simplify to the following set of equations:

$$\epsilon = \frac{19\pi^2}{12} T^4 + 3 \frac{(\mu_B - 2\mu_s)^2 + \mu_s^2}{2} T^2 + 3 \frac{(\mu_B - 2\mu_s)^4 + \mu_s^4}{4\pi^2}, \quad (16)$$

$$n_B = \frac{\mu_B - \mu_s}{3} T^2 + \frac{(\mu_B - 2\mu_s)^3 + \mu_s^3}{3\pi^2}, \quad (17)$$

$$n_Q = \frac{2\mu_B - 5\mu_s}{3} T^2 + \frac{2(\mu_B - 2\mu_s)^3 - \mu_s^3}{3\pi^2}. \quad (18)$$

We refer to the  $T$ ,  $\mu_B$ ,  $\mu_Q$  and  $\mu_s$  values extracted from the  $\epsilon$ ,  $n_B$ , and  $n_Q$  values using Eqs.(15)-(18) as the ‘‘full solution’’ for the quantum ideal gas EoS.

On the other hand, if one ignores the electric charge by setting  $\mu_Q = 0$ , Eq.(15) gives  $\mu_s = \mu_B/3$ , which leads to the following simplified equations:

$$\epsilon_1 = \frac{19\pi^2}{12} T^4 + \frac{\mu_B^2}{3} T^2 + \frac{\mu_B^4}{54\pi^2}, \quad (19)$$

$$n_{B,1} = \frac{2\mu_B}{9} T^2 + \frac{2\mu_B^3}{81\pi^2}. \quad (20)$$

We refer to the  $T$  and  $\mu$  values extracted from the  $\epsilon$  and  $n_B$  values using Eqs.(19)-(20) as the ‘‘partial-1 solution’’ for the quantum EoS. However, note that in this case Eq.(18) would give  $n_Q = n_B/2$ , which is inconsistent with the result  $n_Q = n_B Z/A$  from our semi-analytical model. This discrepancy, which also exists for the Boltzmann statistics, is a consequence of the choice for  $\mu_Q$ . On the other hand, for the Au+Au collisions that we consider in this study,  $Z/A \approx 0.4$  is not far from  $1/2$ .

Additionally, if one ignores both the electric charge and strangeness by setting  $\mu_Q = \mu_s = 0$ , Eqs.(A.5)-(A.6) lead to the following different set of simplified equations:

$$\epsilon_2 = \frac{19\pi^2}{12} T^4 + \frac{\mu_B^2}{2} T^2 + \frac{\mu_B^4}{36\pi^2}, \quad (21)$$

$$n_{B,2} = \frac{\mu_B}{3} T^2 + \frac{\mu_B^3}{27\pi^2}. \quad (22)$$

We refer to the  $T$  and  $\mu$  values extracted from the  $\epsilon$  and  $n_B$  values using Eqs.(21)-(22) as the ‘‘partial-2 solution’’ for the quantum EoS. Note that this approximation is inconsistent with Eq.(15) from our semi-analytical model. In addition, in this case Eqs.(A.7)-(A.8) would give  $n_Q = 0$  and  $n_s = -n_B$  (same for the Boltzmann statistics), which are more inconsistent with the results from our semi-analytical model [20] and the numerical results from the AMPT model study [17].

### C. Thermodynamics of a massless QGP with the Boltzmann EoS

Using Eq.(15) that is also valid for Boltzmann statistics, the general results in Eqs.(A.9)-(A.12) simplify to the following set of equations:

$$\epsilon = \frac{12}{\pi^2} T^4 \left[ 7 + 3 \cosh \left( \frac{\mu_B - 2\mu_s}{T} \right) + 3 \cosh \left( \frac{\mu_s}{T} \right) \right], \quad (23)$$

$$n_B = \frac{4}{\pi^2} T^3 \left[ \sinh \left( \frac{\mu_B - 2\mu_s}{T} \right) + \sinh \left( \frac{\mu_s}{T} \right) \right], \quad (24)$$

$$n_Q = \frac{4}{\pi^2} T^3 \left[ 2 \sinh \left( \frac{\mu_B - 2\mu_s}{T} \right) - \sinh \left( \frac{\mu_s}{T} \right) \right]. \quad (25)$$

They provide the full solution of  $T$  and  $\mu$  for the Boltzmann ideal gas EoS.

Again, if we ignore electric charge by setting  $\mu_Q = 0$ , we then have the following that defines the partial-1 solution for the Boltzmann EoS:

$$\epsilon_1 = \frac{12}{\pi^2} T^4 \left[ 7 + 6 \cosh \left( \frac{\mu_B}{3T} \right) \right], \quad (26)$$

$$n_{B,1} = \frac{8}{\pi^2} T^3 \sinh \left( \frac{\mu_B}{3T} \right). \quad (27)$$

Alternatively, if one sets  $\mu_Q = \mu_S = 0$ , one would simplify Eqs.(A.9)-(A.10) to the following equations that determine the partial-2 solution for the Boltzmann EoS:

$$\epsilon_2 = \frac{12}{\pi^2} T^4 \left[ 4 + 9 \cosh \left( \frac{\mu_B}{3T} \right) \right], \quad (28)$$

$$n_{B,2} = \frac{12}{\pi^2} T^3 \sinh \left( \frac{\mu_B}{3T} \right). \quad (29)$$

#### D. Thermodynamics of the Lattice EoS

A lattice QCD-based EoS [32, 33] provides another way to relate the energy density and net conserved-charge densities  $\epsilon, n$  to the temperature and conserved-charge chemical potentials  $T, \mu$ . First, the pressure is written as a Taylor series in all three  $\mu/T$  up to a total power  $i + j + k \leq 4$  [33]:

$$\frac{p}{T^4} = \sum_{i,j,k} \frac{1}{i!j!k!} \chi_{ijk}^{BQS} \left( \frac{\mu_B}{T} \right)^i \left( \frac{\mu_Q}{T} \right)^j \left( \frac{\mu_S}{T} \right)^k. \quad (30)$$

The coefficients  $\chi_{ijk}^{BQS}$  have been calculated on a  $48^3 \times 12$  lattice in the temperature range  $T \in [135, 220]$  MeV [32]. However, this temperature range is not enough to cover the full hydrodynamical evolution of the matter produced in heavy-ion collisions, so a more complete EoS is constructed [33]. The coefficients are smoothly merged with the results from the hadron resonance gas model [34] to constrain the low temperature behavior of the EoS, while in the high temperature regime each coefficient is imposed to smoothly approach its Boltzmann limit [33]. Except for  $\chi_{200}^{BQS}$ , each coefficient has been written as a ratio of ninth-degree polynomials in inverse powers of a scaled temperature  $T_1 \equiv T/(154 \text{ MeV})$ :

$$\chi_{ijk}^{BQS} = \frac{\sum_n a_n^{ijk} / T_1^n}{\sum_n b_n^{ijk} / T_1^n} + c_0^{ijk}. \quad (31)$$

The susceptibility  $\chi_{200}^{BQS}$  has a different form:

$$\chi_{200}^{BQS} = e^{-h_1/T_2 - h_2/T_2^2} f_3 [1 + \tanh(f_4 T_2 + f_5)], \quad (32)$$

where  $T_2 \equiv T/(200 \text{ MeV})$  [33] is a different scaled temperature. In Eqs.(31) and (32),  $a_n, b_n, c_0, h_1, h_2, f_3, f_4$ , and  $f_5$  are constant coefficients whose values are published [33].

With these parameterizations of  $\chi_{ijk}^{BQS}$ , the pressure is fully defined, and one can use the standard thermodynamic relations to find  $\epsilon, n_B, n_Q$ , and  $n_S$ , and the entropy density  $s$  in terms of  $T$  and  $\mu$ :

$$\begin{aligned} \frac{\epsilon}{T^4} &= \frac{s}{T^3} - \frac{p}{T^4} + \frac{\mu_B}{T} \frac{n_B}{T^3} + \frac{\mu_Q}{T} \frac{n_Q}{T^3} + \frac{\mu_S}{T} \frac{n_S}{T^3}, \\ \frac{n_B}{T^3} &= \frac{1}{T^3} \frac{\partial p}{\partial \mu_B} \Big|_{T, \mu_Q, \mu_S}, \quad \frac{n_Q}{T^3} = \frac{1}{T^3} \frac{\partial p}{\partial \mu_Q} \Big|_{T, \mu_B, \mu_S}, \\ \frac{n_S}{T^3} &= \frac{1}{T^3} \frac{\partial p}{\partial \mu_S} \Big|_{T, \mu_B, \mu_Q}, \quad \frac{s}{T^3} = \frac{1}{T^3} \frac{\partial p}{\partial T} \Big|_{\mu_B, \mu_Q, \mu_S}. \end{aligned} \quad (33)$$

When using this lattice EoS, we impose the conditions relevant to heavy-ion collisions, which are already implemented in our semi-analytical model [19, 20]:

$$n_Q = n_B Z/A, \quad n_S = 0. \quad (34)$$

We can then use our  $\epsilon(t)$  and  $n(t)$  values as inputs to the lattice EoS to extract the corresponding  $T$  and  $\mu$  values, which we refer to as the full solution with the lattice EoS.

Our method of extracting the  $T$  and  $\mu$  values for given  $\epsilon$  and  $n$  values involves calculating the intersection of the corresponding constant  $\epsilon$  and  $n_B$  contours in the  $T - \mu_B$  plane. First we reject any solution that has  $T < 70$  MeV because in this region we find that the energy density reconstructed with Eq.(33) can be negative, which is unphysical. Another complication is that there are often multiple solutions for the  $T$  and  $\mu$  values (for a given set of  $\epsilon$  and  $n$  values). There is often a branch of solutions at  $\mu_B \gtrsim 2$  GeV and  $T \gtrsim 500$  MeV; we reject these solutions since they occur well beyond the expected region of validity of the lattice QCD calculations ( $\mu_B/T \lesssim 2.5$ ) [33]. At lower collision energies, the numerical solutions of the trajectory often form two branches: the first behaving as expected, while the second lies at lower  $T$  and higher  $\mu_B$ . We reject the second branch because it has larger  $\mu_B/T$  values; in addition, that branch occurs near or below  $T \sim 135$  MeV where the lattice QCD calculations stop [32]. As a result, at  $\sqrt{s_{NN}} = 2.0$  GeV we find no  $T$  and  $\mu$  solutions for the densities at any time during the evolution. For  $\sqrt{s_{NN}} \gtrsim 4.0$  GeV, the trajectory can be extracted with the lattice EoS, although at low energies (i.e., energies not much higher than 4 GeV) only a portion of the trajectory around the time of  $\epsilon^{\max}$  can be extracted.

### III. RESULTS

#### A. Energy and net-baryon density

Figure 1 shows the results of  $\epsilon(t)$  and  $n_B(t)$  at mid-spacetime-rapidity averaged over the full transverse overlap area for central Au+Au collisions at three different energies. The results from our semi-analytical model at

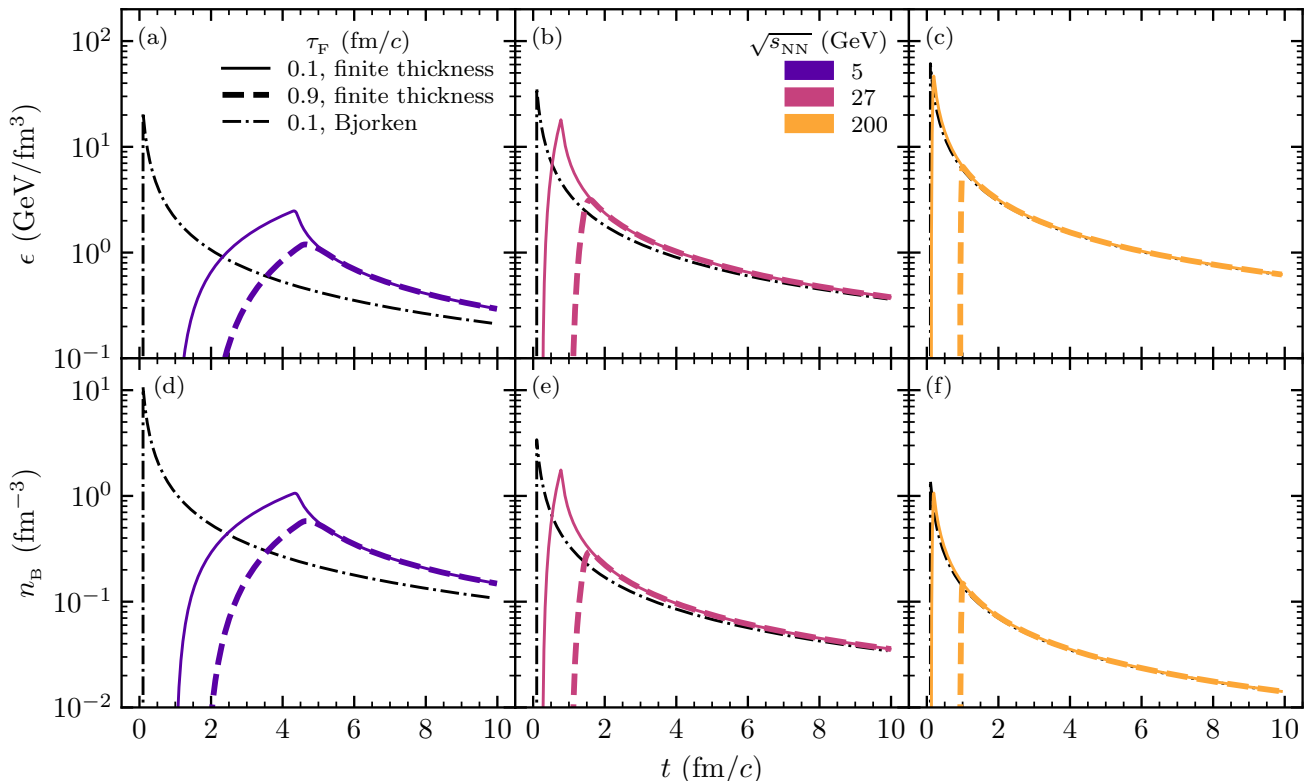


FIG. 1: (a-c) Energy density  $\epsilon(t)$  and (d-f) net-baryon density  $n_B(t)$  at mid-spacetime-rapidity averaged over the full transverse area for central Au+Au collisions at  $\sqrt{s_{NN}} = 5.0, 27,$  and  $200$  GeV from our model with  $\tau_F = 0.1$  (solid) and  $0.9$  (dashed) fm/c in comparison with results from the Bjorken formula with  $\tau_F = 0.1$  fm/c (dot-dashed).

$\tau_F = 0.1$  and  $0.9$  fm/c are shown together with the results from the Bjorken energy density formula at  $\tau_F = 0.1$  fm/c. We observe that the peak energy density  $\epsilon^{\max}$  from our model increases as  $\sqrt{s_{NN}}$  increases, while the peak net-baryon density  $n_B^{\max}$  mostly decreases with  $\sqrt{s_{NN}}$  (except for an increase at low to moderate  $\sqrt{s_{NN}}$  and small  $\tau_F$ ).

We also see the large effect that the finite nuclear thickness has on the predicted densities at low collision energies [19, 20]. Compared to the results from the Bjorken formula [18], our results from Eq.(2) and Eq.(12) have significantly smaller  $\epsilon^{\max}$  and  $n_B^{\max}$  at low collision energies, while the difference from the Bjorken results decreases and eventually vanishes at high collision energies as expected. Note that we use  $dm_T/dy$  of Eq.(4) for the  $dE_T/dy$  term in Eq.(1) to calculate the Bjorken energy density as  $\epsilon^{Bj}(t) = 1/(A_T t) dm_T/dy$ , and the net-baryon density in the Bjorken formula is given by

$$n_B^{Bj}(t) = \frac{1}{A_T t} \frac{dN_{\text{netB}}}{dy}. \quad (35)$$

Figure 1 also shows the  $\tau_F$ -dependence of the densities, where  $\epsilon^{\max}$  and  $n_B^{\max}$  are lower and occur later in time at a larger  $\tau_F$ . In addition, the late time evolution of the densities approaches the Bjorken results for all  $\tau_F$

and does so earlier in time for higher collision energies. Therefore, we expect significant differences in the  $T - \mu_B$  trajectories at low energies between our results and the results from the Bjorken formula. Note that at late times ( $t \geq t_2 + \tau_F$ ) our energy density and net-baryon densities do not depend on the formation time, because the integration limits of  $x$  and  $z_0$  at late times are independent of  $\tau_F$  as shown in piece III of Table I. Also, due to  $v_z = (z - z_0)/(t - x)$ , at late times only partons with  $y \sim 0$  will contribute to the densities at  $z = 0$  (regardless of their production point), which is the same as for the Bjorken densities. Therefore, at late times our densities approach the results from the Bjorken density formulae.

We also note that the densities of our semi-analytical model can decrease at a faster rate just after the time of maximum density than the densities from the Bjorken formulae; this is more noticeable at lower collision energies. The decrease of our energy and net-baryon densities with time can be understood analytically because they are similar to the results calculated using a uniform time profile [19]. There, the densities decrease with time as  $\ln[(t - t_1)/(t - t_2)]$  for  $t \geq t_2 + \tau_F$  after the maximum density is reached. Therefore, at the beginning of the decreasing part of the curve (i.e., at  $t$  just after  $t_2 + \tau_F$ ), our densities decrease as  $\ln[1/(t - t_2)]$ , which is faster than

the  $1/t$  behavior of the Bjorken densities at the same  $t$ . On the other hand, this can also be seen as a simple shift of time (i.e., from  $t$  to  $t - t_2$ ) due to the finite nuclear thickness.

In addition, we notice that the maximum density at a given collision energy for a larger  $\tau_F$  is almost on the tail part of the density curve for a smaller  $\tau_F$ . Again, we can understand this merging of the late time evolutions of the energy and net-baryon densities by considering the case of the densities calculated using a uniform time profile [19]. At late times after the time of maximum density, the uniform time profile gives densities which are proportional to  $\ln[(t - t_1)/(t - t_2)]$ , which does not involve  $\tau_F$ . Therefore, the late time evolutions from our model are independent of  $\tau_F$ .

### B. Trajectory of a massless QGP with the quantum EoS

In Fig. 2, we show the  $T$  and  $\mu$  results extracted using the full solution, the partial-1 solution, and the partial-2 solution of the quantum EoS, in comparison with the results extracted using the lattice EoS. We see that  $T^{\max}$  increases with  $\sqrt{s_{\text{NN}}}$ , while  $\mu_B^{\max}$  decreases with  $\sqrt{s_{\text{NN}}}$  (from 5 GeV) for all four equations of state. It is obvious that both  $T$  and  $\mu_B$  reach the peak value earlier in time at higher energies due to the shorter duration time  $d_t$ . Figure 2 also shows that the partial-1 solution reproduces the  $T(t)$  and  $\mu_B(t)$  results from the full solution almost exactly over the entire time evolution. On the other hand, the partial-2 solution gives a much smaller  $\mu_B$  than the full solution. In addition, we see that the magnitude of  $\mu_Q$  in the full solution is very small ( $\lesssim 30$  MeV), so the assumption  $\mu_Q = 0$  in both the partial-1 and partial-2 solutions is reasonable for the ideal gas EoS. Furthermore,  $\mu_s \simeq \mu_B/3$  in the full solution explains why the partial-1 solution that assumes  $\mu_s = \mu_B/3$  is much better than the partial-2 solution that assumes  $\mu_s = 0$ . We note that the recent numerical results from the AMPT model for the ideal gas EoS [17] also show  $\mu_Q \approx 0$  and  $\mu_s \approx \mu_B/3$ .

Figure 3 shows the  $T - \mu_B$  trajectories in the QCD phase diagram for the quantum EoS with  $\tau_F = 0.3$  fm/c. At very early times  $t \in [0, t_1 + \tau_F)$ , the system is at  $(\epsilon, n_B) = (0, 0)$ , which corresponds to  $(\mu_B, T) = (0, 0)$  for the ideal gas EoS. For  $\sqrt{s_{\text{NN}}} \gtrsim 4$  GeV, the trajectories pass through the crossover curve, which comes from calculations using the functional renormalization group (FRG) with  $N_F = 2 + 1$  [35]. When a given trajectory reaches its endpoint, which corresponds to the time when both  $\epsilon^{\max}$  and  $n_B^{\max}$  are reached, it turns clockwise and returns toward the origin. At high collision energies, the returning part of the trajectory is so close to the outgoing part that the two appear to overlap. At low energies such as  $\sqrt{s_{\text{NN}}} = 5.0$  GeV, however, the two parts are distinguishable. This behavior can be understood with the uniform time profile for the density production [19]. In

this case, both densities have the same time evolution and differ only in their constants of proportionality. Therefore, the time evolution of the energy and net-baryon densities in our model are expected to be quite similar at all times. Hence, the returning part of a trajectory should thus overlap with the outgoing part because, for two points (one on the increasing part and the other on the decreasing part) in a trajectory with the same energy density, the net-baryon densities will also be very similar.

Notably, at  $\sqrt{s_{\text{NN}}} \gtrsim 4.4$  GeV both the outgoing and returning parts of the trajectory intersect the FRG crossover curve, while at  $\sqrt{s_{\text{NN}}} \lesssim 3.6$  GeV, neither part of the trajectory intersects the FRG crossover curve. In Fig. 3, we also see that the trajectories from the partial-1 solution match quite closely those from the full solution. We have also used Eq.(19) from the partial-1 solution for the quantum EoS to calculate the lines of constant  $\epsilon$  that go through the two endpoints of the FRG crossover curve. They correspond to  $\epsilon = 0.51$  and  $1.23$  GeV/fm<sup>3</sup>, as shown in Fig. 3.

The results from our semi-analytical model [20] depend on the value of  $\tau_F$ , and Fig. 4 shows how the  $T - \mu_B$  trajectories from the quantum EoS full solution depend on  $\tau_F$ . As  $\tau_F$  decreases, the trajectory becomes longer with the endpoint moving further to higher  $\mu_B$  (and also higher  $T$  except at very low energies). Note that the trajectory endpoint corresponds to both  $\epsilon^{\max}$  and  $n_B^{\max}$ , but at low energies it does not necessarily correspond to both  $T^{\max}$  and  $\mu_B^{\max}$ ; this can be seen from the 2 GeV curve in Fig. 4. We also see that the outgoing parts of the trajectories at a given collision energy but different  $\tau_F$  sometimes do not overlap well, consistent with the significant dependence of  $\epsilon(t)$  and  $n_B(t)$  on  $\tau_F$  at early times as shown in Fig. 1. On the other hand, the returning parts of the trajectories overlap well, because  $\epsilon(t)$  and net conserved-charge densities at late times are insensitive to  $\tau_F$ .

We have also calculated how the endpoint of a trajectory depends on the collision energy at given formation times in Fig. 4. At high collision energies, we observe a clear separation of the endpoint curves for different  $\tau_F$  values. At very low collision energies, however, this separation decreases [19, 20]. The sensitivity of the trajectory endpoint to  $\tau_F$  can be understood in terms of the simpler uniform time profile [19], which have maximum values proportional to  $\ln(1 + t_{21}/\tau_F)$ . Note that the endpoint of a trajectory corresponds to the maximum values of the energy and net-baryon densities. At high collision energies where  $t_{21}/\tau_F \ll 1$ , the maximum densities are inversely proportional to  $\tau_F$  since  $\ln(1 + t_{21}/\tau_F) \sim t_{21}/\tau_F$ , so they are very sensitive to the  $\tau_F$  value. On the other hand, at low collision energies where  $t_{21}/\tau_F \gg 1$ , the maximum densities scale roughly as  $\ln(t_{21}/\tau_F)$ , so they are much less sensitive to the value of  $\tau_F$ . Therefore, the endpoint is more sensitive to the value of the formation time at high collision energies than at low collision energies.

At the threshold energy  $E_0$ , the endpoint curves at different  $\tau_F$  converge to the same endpoint, which is lo-

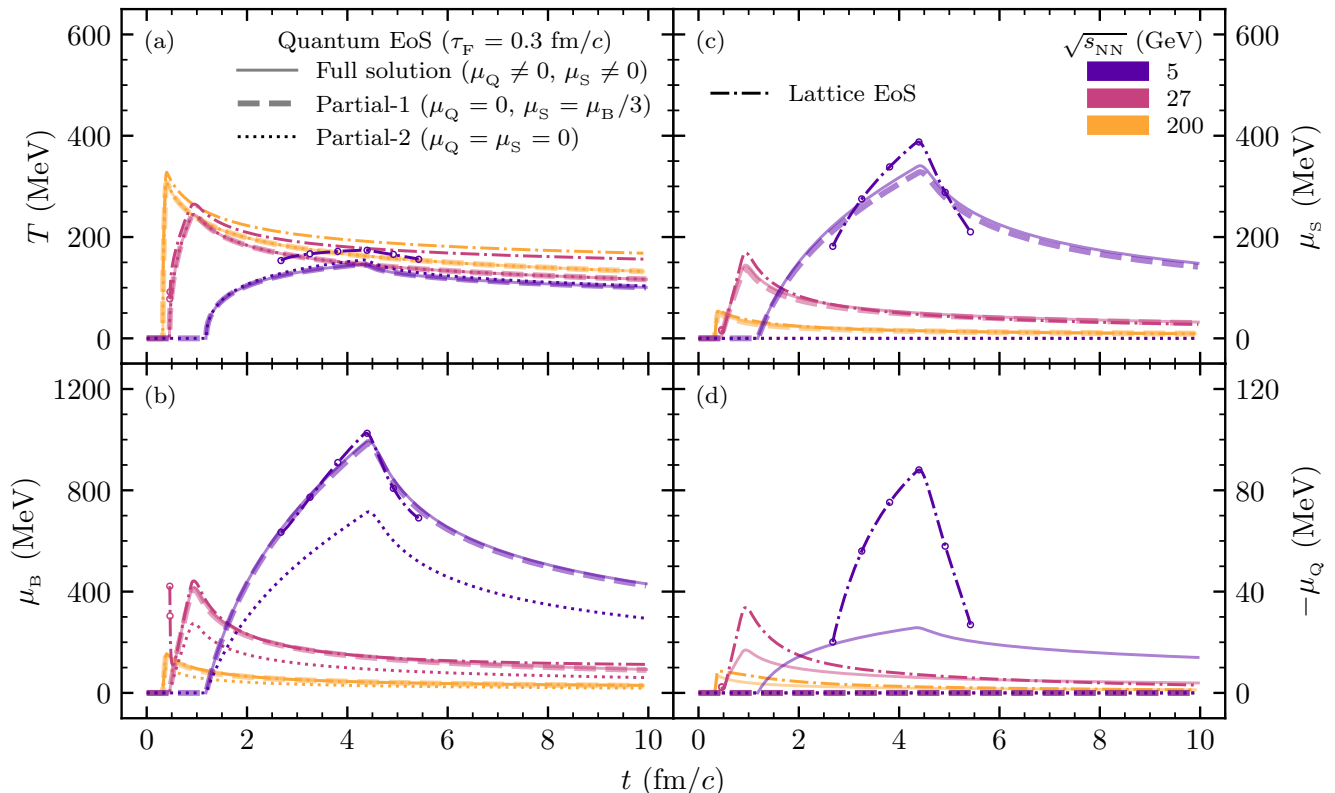


FIG. 2: (a)  $T(t)$ , (b)  $\mu_B(t)$ , (c)  $\mu_S(t)$ , and (d)  $-\mu_Q(t)$  for a massless QGP with the quantum EoS using the full (solid), partial-1 (dashed), and partial-2 (dotted) solutions in comparison with results using the lattice EoS (dot-dashed). Open circles on the lattice curves represent times for which the corresponding trajectory has  $\mu_B/T > 2.5$  and thus may be unreliable. All results are for central Au+Au collisions at  $\sqrt{s_{\text{NN}}} = 5.0, 27, \text{ and } 200$  GeV with  $\tau_F = 0.3$  fm/c.

cated at  $(\mu_B, T) \sim (900 \text{ MeV}, 60 \text{ MeV})$ . We also see that the CEP from the FRG calculation [35] at  $(\mu_B, T) = (635 \text{ MeV}, 107 \text{ MeV})$  is well within the endpoint curves (even for  $\tau_F = 0.9$  fm/c), which means that this CEP location should be accessible with central Au+Au collisions. On the other hand, the  $T - \mu_B$  region below the  $\sqrt{s_{\text{NN}}} = 2$  GeV trajectory in the QCD phase diagram is essentially inaccessible to central Au+Au collisions according to our model.

Note that our semi-analytical model should break down at very low energies because the initial matter after the primary collisions would not be in parton degrees of freedom. In fact, our semi-analytical model predicts that the trajectories for ideal gas equations of state start at the origin of the QCD phase diagram and return toward it precisely because we assume the system is always in the parton phase. It would be nice to further improve our model to incorporate the energy loss of the participant nucleons or the interaction among secondary particles, which are beyond the scope of this study. We have neglected secondary particles and their interactions in order to analytically solve the resulting equations and get a reasonable analytical solution of the trajectory. On the other hand, these effects have been

included in the AMPT model calculations of the collision trajectories [17]. Those AMPT model results and our semi-analytical results share many of the same qualitative features of the trajectories for ideal gas EoS.

Since our model gives  $\epsilon^{\text{max}} = 2\rho_0 m_N$  and  $n_B^{\text{max}} = 2\rho_0$  at the threshold energy as one naively expects, the  $\epsilon$  and  $n_B$  values at very low energies from our model should not be far off. However, below the crossover curve, one expects the system to freeze out and behave like a hadron resonance gas. Therefore, the trajectories from the EoS of an ideal gas of massless partons well below the crossover curve (or the first-order phase transition line beyond the CEP) are not reliable.

### C. Trajectory of a massless QGP with the Boltzmann EoS

We show in Fig. 5 the time evolutions of  $T$  and  $\mu$  extracted using the full solution, the partial-1 solution, and the partial-2 solution of the Boltzmann ideal gas EoS for a massless QGP. Similar to the results for the quantum EoS shown in Fig. 2, the full and partial-1 solutions give essentially the same results, while the partial-2 solution



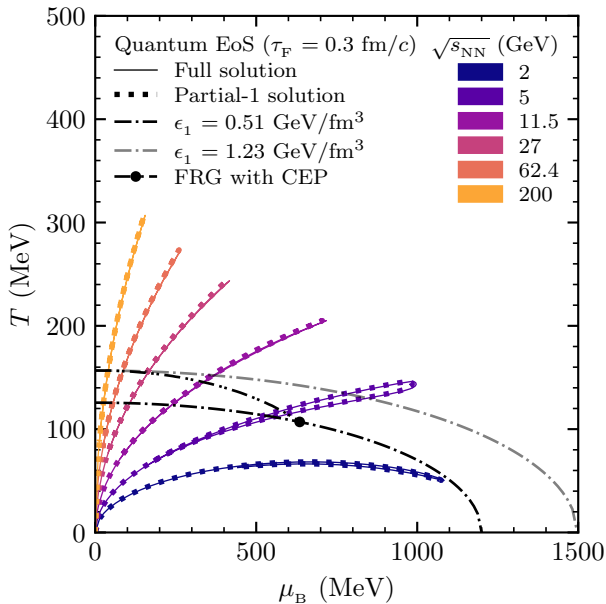


FIG. 3: Trajectories for a massless QGP with the quantum EoS for the full (solid) and partial-1 (dotted) solutions with  $\tau_F = 0.3$  fm/c for central Au+Au collisions at  $\sqrt{s_{NN}} = 2.0, 5.0, 11.5, 27.0, 62.4,$  and  $200$  GeV. Two constant energy density lines from the partial-1 solution (dot-dashed) and the FRG crossover curve (dash-dot-dot) with the CEP (filled circle) are also shown for reference.

gives significantly smaller  $\mu_B$  values. In addition, the magnitudes of  $\mu_Q$  from the full solution of the Boltzmann EoS are even smaller than those for the quantum EoS. As a result,  $\mu_S \simeq \mu_B/3$  also holds for the full solution here.

Figure 6 shows how the  $T - \mu_B$  trajectories using the full solution of the Boltzmann EoS depend on  $\tau_F$ . We observe the same behavior as for the quantum EoS. The trajectory endpoint at the threshold energy is obtained by using the partial-1 solution for the Boltzmann EoS with  $e^{\max} = 2\rho_0 m_N$  and  $n_B^{\max} = 2\rho_0$ , and it now lies to the left of the CEP. We also show the two lines of constant  $\epsilon$  as calculated from the partial-1 solution of Eq.(26) for the Boltzmann EoS, which go through the endpoints of the FRG crossover curve. Interestingly, they both show a half-loop structure, which is totally different from the shape of constant- $\epsilon$  lines for the quantum EoS. We can understand this by considering the total differential for Eq.(26):  $d\epsilon_1 = \partial_T \epsilon_1 dT + \partial_{\mu_B} \epsilon_1 d\mu_B$ . At constant energy density where  $d\epsilon_1 = 0$ , we find

$$\frac{d\mu_B}{dT} = -\frac{\partial_T \epsilon_1}{\partial_{\mu_B} \epsilon_1}. \quad (36)$$

The numerator in the above equation is zero when  $\mu_B/(3T) \approx 4.15$ , which corresponds to the turning point in the line of constant energy density for the Boltzmann EoS. If one follows a line of constant  $\epsilon$  starting from the

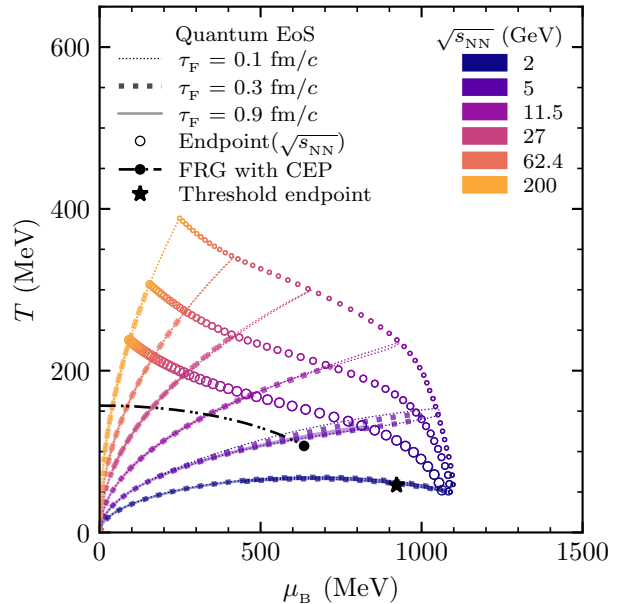


FIG. 4: Trajectories for the quantum EoS with  $\tau_F = 0.1$  (thin dotted),  $0.3$  (thick dotted), and  $0.9$  (solid) fm/c for central Au+Au collisions at  $\sqrt{s_{NN}} = 2.0, 5.0, 11.5, 27.0, 62.4,$  and  $200$  GeV, together with the trajectory endpoint curves (open circles) as functions of  $\sqrt{s_{NN}}$ . The FRG crossover curve (dash-dot-dot) with the CEP (filled circle) and the endpoint at the threshold energy (star) are also shown for reference.

higher-temperature side at  $\mu_B = 0$  (where  $\epsilon \gg n_B m_N$ ), one will arrive at a point (near the turning point) beyond which  $\epsilon < n_B m_N$ . Since it is unnatural for a nuclear matter including the QGP to have  $\epsilon < n_B m_N$  if baryon number is effectively related to the baryon mass, the  $T - \mu_B$  points on the lower part (roughly the lower half) of each constant- $\epsilon$  curve in Fig. 6 do not represent a physical QGP system with the Boltzmann EoS.

Figure 6 also shows how the endpoint of a trajectory depends on the collision energy at a given formation time. As in Fig. 4, at high collision energies we see a clear separation of the endpoint curves for different formation times. Notably, the CEP from the FRG calculation is now much closer to the  $\tau_F = 0.9$  fm/c endpoint curve than the quantum EoS case. Another key difference between Figs. 6 and 4 is the location of the CEP with respect to individual trajectories. For the Boltzmann EoS shown in Fig. 6, the CEP lies close to the returning part of the 3.2 GeV trajectory or the outgoing part of the 2.8 GeV trajectory. For the quantum EoS shown in Fig. 4, the CEP is close to the returning part of the 4.4 GeV trajectory or the outgoing part of the 3.6 GeV trajectory.

In Fig. 7, we compare our results with the  $T - \mu_B$  trajectories that are extracted from the  $\epsilon(t)$  and  $n_B(t)$  values calculated with the Bjorken formula [18]. At high collision energies, the trajectories from the Bjorken formula are rather close to our results that include the finite

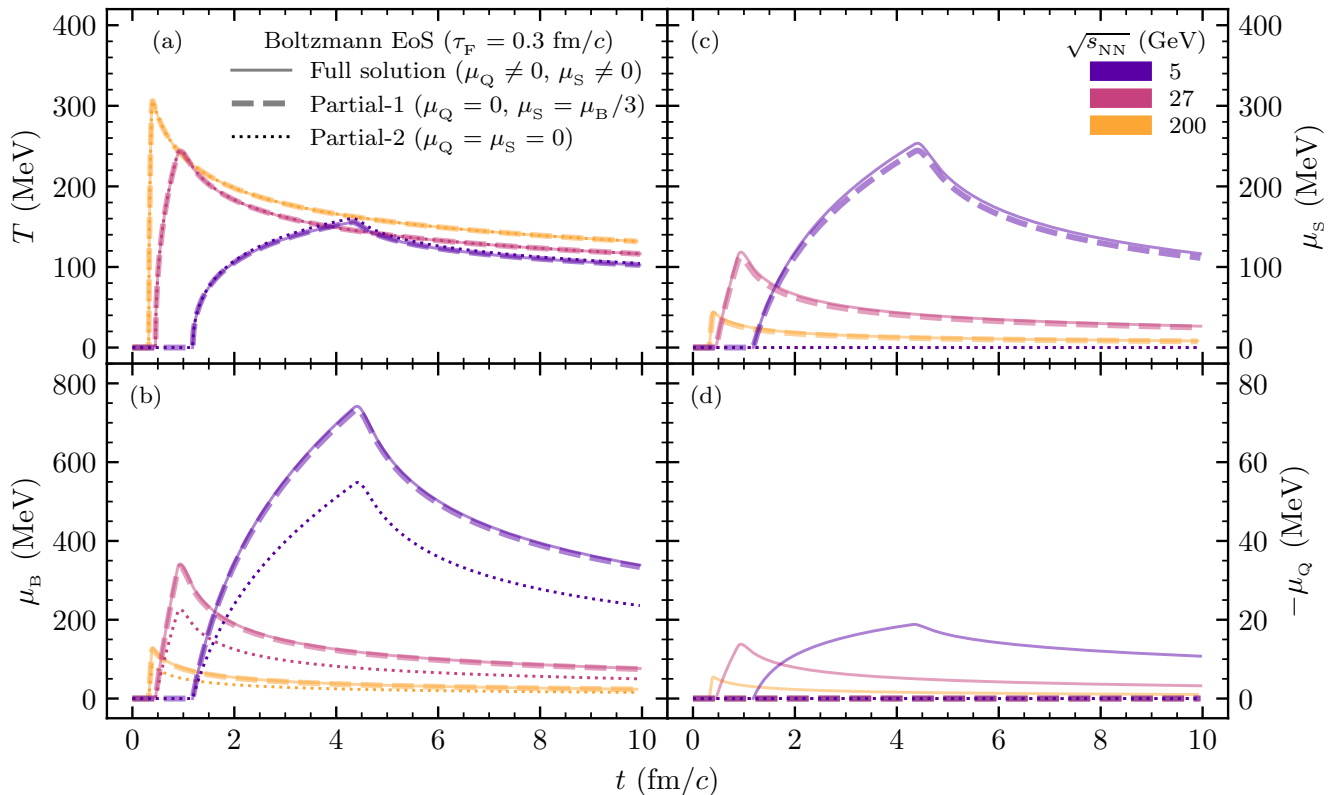


FIG. 5: Same as Fig. 2, but for the Boltzmann EoS and without the lattice EoS results.

nuclear thickness for the same (quantum) EoS, as expected. At lower collision energies, however,  $\mu_B^{\max}$  from the Bjorken formula is much larger, and there is no outgoing part of the trajectory since  $\epsilon^{\max}$  and  $n_B^{\max}$  in the Bjorken formula occur at the earliest time ( $t = \tau_F$ ). In contrast, in our semi-analytical model the time of maximum density occurs much later, sometime within the range  $[t_a, t_2 + \tau_F]$  [20]. We also observe in Fig. 7 that the late-time part of a trajectory from the Bjorken formula overlaps with the returning part of our trajectory. This is because the Bjorken formula and our semi-analytical model predict the same densities at late times [19, 20], which can be seen in Fig. 1.

At low collision energies we observe a problem in extracting the trajectory when using the Bjorken densities and the quantum EoS, in that sometimes no solution for the  $T - \mu_B$  trajectory exists at early times. For example, at  $\sqrt{s_{NN}} = 2$  GeV and  $\tau_F = 0.3$  fm/c, no solution is found before  $t \sim 8$  fm/c, at which time  $\mu_B^{\max} \sim 1300$  MeV and  $T \sim 0$  MeV; afterwards the Bjorken trajectory rises in  $T$  and decreases in  $\mu_B$  approaching the returning part of the trajectory that is extracted using the densities from our semi-analytical model. This problem occurs more often at low energies and small formation times, while it does not occur for collision energies higher than  $\sim 5$  GeV at  $\tau_F = 0.3$  fm/c. Note that this problem also does not occur for the Boltzmann EoS [36]. To

understand this problem, we can use the partial-1 solution of the quantum EoS in Eqs.(19)-(20), which give  $\epsilon^{1/4}/n_B^{1/3} \geq (2187\pi^2/128)^{1/12} \simeq 1.533$ , where the equal sign corresponds to the solution at  $T = 0$ . On the other hand, since the peak Bjorken energy and net-baryon densities both change as  $1/\tau_F$ ,  $\epsilon^{1/4}/n_B^{1/3} \propto \tau_F^{1/12}$  will decrease to the above value of 1.533 at a certain finite  $\tau_F$  value. When we decrease  $\tau_F$  further, there will be no ( $T \geq 0, \mu_B$ ) solution anymore. Note that these scaling relations of the Bjorken density formulae are not all the same as the those in the Bjorken hydrodynamics picture that has  $n \propto 1/\tau_F$  but  $\epsilon \propto 1/\tau_F^{4/3}$ .

We also see in Fig. 7 that the magnitude of the net-baryon chemical potential can be large, even higher than 2 GeV. Using the Bjorken densities and the partial-1 solution of the quantum EoS in Eqs. (19)-(20), one can show analytically that the baryon chemical potential has no upper limit in the parton phase. As an example, let us consider the peak Bjorken densities at  $\tau_F = 0.3$  fm/c at 27 GeV, which essentially corresponds to the endpoint of the dashed magenta trajectory in Fig. 7. If we decrease  $\tau_F$ , it is straightforward to show with Eqs. (19)-(20) that the trajectory endpoint will move to the right to reach a higher  $\mu_B$  while the  $T/\mu_B$  ratio will decrease. Therefore, the maximum baryon chemical potential  $\mu_B^{\max}$  for a Bjorken trajectory at a given energy (for all  $\tau_F$  values) is reached at  $T = 0$ , where the partial-1 solution of the

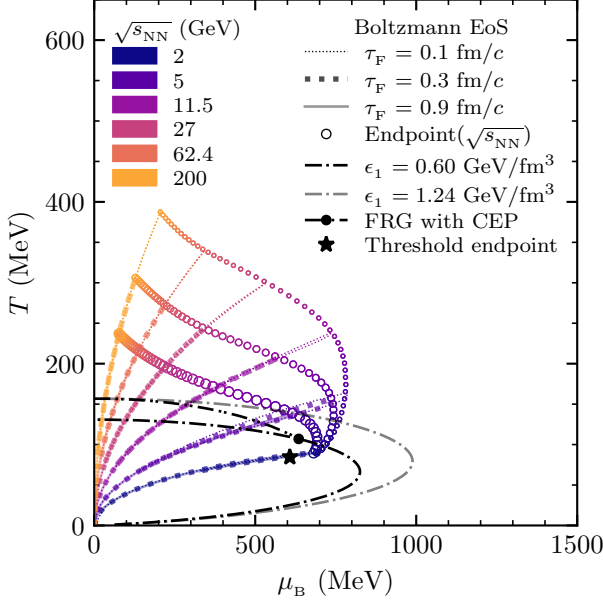


FIG. 6: Same as Fig. 4, but for the Boltzmann EoS.

quantum EoS in Eqs. (19)-(20) gives

$$\frac{\epsilon}{n_B} = \frac{3}{4} \mu_B^{\max}. \quad (37)$$

In our model, the Bjorken energy and net-baryon densities satisfy the following inequality because of Eq.(4):

$$\frac{\epsilon}{n_B} = m_N + \frac{dE_T/dy}{dN_{\text{netB}}/dy} \geq m_N.$$

The above two relations then give

$$\mu_B^{\max} \geq 4m_N/3 \simeq 1.25 \text{ GeV}.$$

Indeed, we can see from Fig. 7 that the 2 GeV Bjorken trajectory reaches the  $T = 0$  axis at a  $\mu_B^{\max}$  value close to 1.25 GeV. At higher energies, the  $\mu_B^{\max}$  value (at  $T = 0$ ) will be even higher.

Comparing our results for the two ideal gas equations of state in Fig. 7, we see that, while the  $T^{\max}$  values are often similar at the same collision energy (except at very low energies), the  $\mu_B^{\max}$  value is significantly larger in the quantum EoS than in the Boltzmann EoS. This feature is also seen in numerical results from the AMPT model [17] and can be understood in terms of the Pauli exclusion principle in quantum statistics. In terms of the thermodynamics relations, this can be understood by examining the first two terms in the Taylor expansion of Eq.(27):  $n_{B,1} \simeq 8\mu_B T^2/(3\pi^2) + 4\mu_B^3/(81\pi^2)$ . The coefficient of each term in the above equation is larger than the corresponding coefficient in Eq.(20) for the quantum EoS. As a result, when the same  $n_B$  is used and the  $T$  values are similar for the two equations of state,  $\mu_B$  for the quantum EoS will be larger.

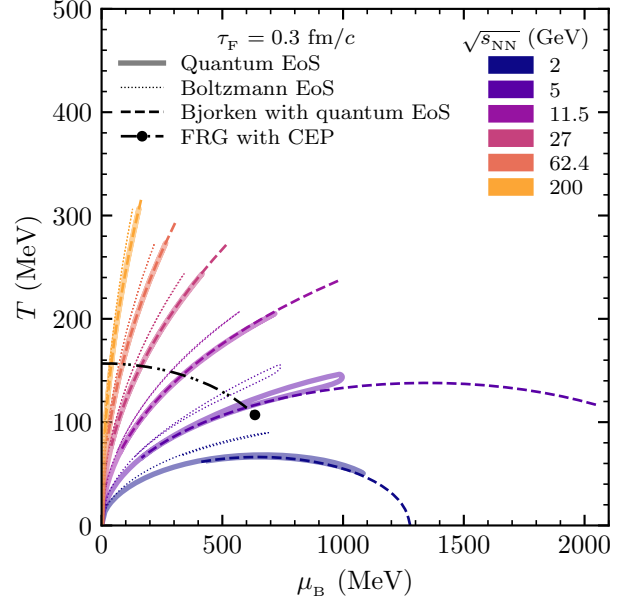


FIG. 7: Trajectories for a massless QGP from the quantum EoS (solid) and the Boltzmann EoS (dotted) using our  $\epsilon(t)$  and  $n_B(t)$  in comparison with those from the quantum EoS using  $\epsilon^{Bj}(t)$  and  $n_B^{Bj}(t)$  (dashed) at  $\tau_F = 0.3 \text{ fm}/c$  for central Au+Au collisions at various energies. The FRG crossover curve (dash-dot-dot) with the CEP is also shown for reference.

#### D. Trajectories of the lattice-QCD EoS

In Fig. 2, we see that the lattice EoS results have a larger  $T$  than the results from the ideal gas EoS, which will lead to significantly longer QGP lifetimes as we shall show in Fig. 10. At low collision energies, no  $T - \mu$  solution for the lattice EoS can be found that corresponds to the  $\epsilon$  and  $n_B$  values at certain times. This can be clearly seen in the 5 GeV results, which do not have solutions at early times or late times. Moreover, the 5 GeV solutions that are found have a  $\mu_B/T > 2.5$  (as indicated by circles on the curve), where we expect the lattice EoS to be unreliable [33]. Note that  $\mu_B$  can first decrease at very early times because the lattice EoS trajectories typically start at a finite  $(\mu_B, T)$  instead of the origin. We also see in Fig. 2 that, while the  $\mu_S$  value extracted with the lattice EoS is reasonably close to the full solution of the quantum EoS, the value of  $\mu_Q$  from the lattice EoS is significantly larger.

We compare in Fig. 8 the trajectories extracted using the full solutions of the quantum EoS and the lattice QCD-based EoS for  $\tau_F = 0.3 \text{ fm}/c$  for central Au+Au collisions. Compared to the quantum EoS, we see that  $T^{\max}$  from the lattice EoS is larger for all collision energies, while  $\mu_B^{\max}$  is slightly smaller at high collision energies but significantly larger at low collision energies. In addition, the point at which the  $T - \mu_B$  trajectory intersects the FRG crossover curve shifts to smaller  $\mu_B$ ,

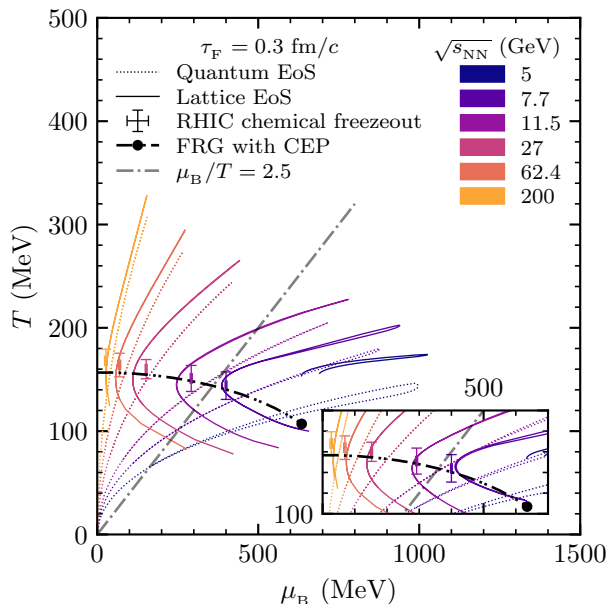


FIG. 8: Trajectories from the quantum EoS (dotted) and the lattice EoS (solid) at  $\tau_F = 0.3$  fm/c for central Au+Au collisions at various energies. The FRG crossover curve (dash-dot) with the CEP (circle) and the  $\mu_B/T = 2.5$  line are shown for reference, and the error-bar markers represent the RHIC chemical freezeout data. The inset shows the trajectories using the previous  $dN_{\text{netB}}/dy$  parameterization [20].

where the shift at high energies is less noticeable than that at lower energies. Furthermore, the trajectory from the lattice EoS bends below the crossover curve because of the smooth transition of the lattice EoS to the hadron resonance gas model at low temperatures.

Figure 8 also shows the chemical freezeout data [37] extracted from grand canonical fits to the particle yields, and we see that they are rather close to the intersection points of our lattice EoS trajectories with the FRG crossover curve. We note that the trajectories and intersection points depend on the parameterization of  $dN_{\text{netB}}/dy$ . In the inset of Fig. 8, we show the trajectories that used the previous  $dN_{\text{netB}}/dy$  parameterization in Ref. [20], which appear to be closer to the RHIC chemical freezeout data. In the region of small  $\mu_B/T$ , which corresponds to moderate to high energies, the lattice EoS trajectories should be more realistic than trajectories from the quantum or Boltzmann ideal gas EoS. In the region of large  $\mu_B/T$ , however, the lattice EoS is expected to be unreliable, for example, we see in Fig. 8 that the trajectory from the lattice EoS at  $\sqrt{s_{\text{NN}}} = 5.0$  GeV has no part below the FRG crossover curve. In such cases, which corresponds to low energies, the ideal gas EoS can still be used to calculate  $T - \mu_B$  trajectories.

## E. Transverse Expansion

To investigate the effect of transverse expansion, we first assume that the radius of the transverse area  $R_T$  in central A+A collisions increases with time as

$$R_T(t) = R_A + \beta_T(t) (t - t_1 - \tau_F), \quad (38)$$

where the transverse flow velocity is modeled as

$$\beta_T(t) = \begin{cases} 0, & \text{for } t < t_1 + \tau_F \\ [1 - e^{-(t-t_1-\tau_F)/t_T}] \beta_{T,f}, & \text{for } t \geq t_1 + \tau_F. \end{cases} \quad (39)$$

We parameterize the final value of the transverse flow velocity  $\beta_{T,f}$  as

$$\beta_{T,f} = \left[ \frac{\ln(\sqrt{s_{\text{NN}}}/E_0)}{64.7 + \ln(\sqrt{s_{\text{NN}}}/E_0)} \right]^{0.202}. \quad (40)$$

The above parameterization uses the kinetic freezeout parameters obtained by fitting the transverse momentum spectral shapes in central Au+Au collisions from 7.7 to 200 GeV and Pb+Pb collisions at 2.76 TeV to a blast-wave model [37–39]. For the low energy behavior, we assume  $\beta_{T,f} \rightarrow 0$  as  $\sqrt{s_{\text{NN}}} \rightarrow E_0$  and use the kinetic freezeout parameters reported in Ref. [37], which contained various data [23, 24, 40–49].

Next, we parameterize  $t_T$ , the timescale for the development of transverse flow, by assuming  $t_T \propto 1/n^{\text{max}}$ , with  $n^{\text{max}}$  being the parton number density at  $\epsilon^{\text{max}}$ , since the mean-free-path of a parton is inversely proportional to the parton number density. For simplicity, we calculate  $n^{\text{max}}$  with the Boltzmann EoS relation,  $n = \sqrt[4]{52\epsilon^3/27/\pi^2}$ , and adopt the following  $\epsilon^{\text{max}}$  that assumes a uniform production profile in time [19]:

$$\epsilon_{\text{uni}}^{\text{max}} = \frac{1}{\pi R_A^2 (t_2 - t_1)} \frac{dm_T}{dy}(0) \ln\left(1 + \frac{t_2 - t_1}{\tau_F}\right). \quad (41)$$

Note that in the above equation we take  $t_1$  and  $t_2$  as  $0.264d_t$  and  $0.736d_t$ , respectively, so that the uniform time profile matches the mean and standard deviation of time as the uniform  $g(z_0, x)$  and Eq.(8) used by our semi-analytical model. We then normalize  $t_T$  to a given value  $t_T^{\text{norm}}$  at  $\sqrt{s_{\text{NN}}} = 200$  GeV and  $\tau_F = 0.3$  fm/c, and we shall vary  $t_T^{\text{norm}}$  from 1 to 6 fm/c.

Figure 9 shows the  $T - \mu_B$  trajectories after including the transverse expansion with  $t_T^{\text{norm}}$  of 1 or 6 fm/c (solid), where the area between the two solid curves at each collision energy is shaded to show the range of the effect of transverse expansion. The trajectories without transverse expansion are also shown (dashed), which corresponds to the case of transverse expansion with  $t_T^{\text{norm}} \rightarrow \infty$ . We see that the path of the trajectory in the QCD phase diagram changes little when including the effect of transverse expansion for all collision energies. Instead, the endpoint of the trajectory shifts closer to the origin (more noticeable at low energies), qualitatively similar to the effect of a larger  $\tau_F$ .

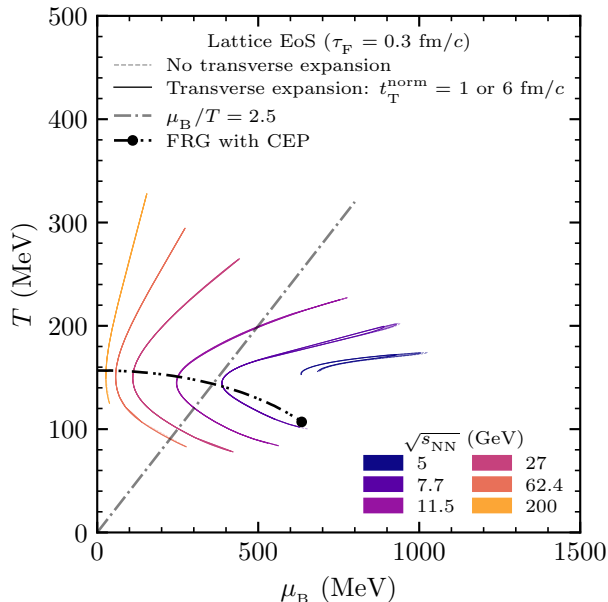


FIG. 9: Trajectories from the lattice EoS without (dashed) or with transverse expansion (solid) at  $\tau_F = 0.3$  fm/c for Au+Au collisions at various energies. The FRG crossover curve (dash-dot-dot) with the CEP (circle) and the  $\mu_B/T = 2.5$  line are also shown for reference.

The small effect of transverse expansion on the trajectories can be understood as follows. Our implementation of transverse expansion is done via a time-dependent transverse area  $A_T(t)$  that increases with a timescale  $t_T$ . At early times (i.e., when  $t - t_1 - \tau_F < t_T$ ), the transverse flow has not developed much, thus transverse expansion has little effect on the densities and the trajectory (typically the outgoing part). At late times (i.e., when  $t - t_1 - \tau_F > t_T$ ), transverse expansion decreases the energy density and net-baryon density by the same factor. When we neglect the transverse expansion, the late time evolution of densities in our model approaches that from the Bjorken formula and decrease as  $1/t$ ; therefore they also decrease with time at the same rate. This means that the late time densities (and thus the trajectory point) with transverse expansion at time  $t$  is the same as the trajectory without transverse expansion at a later time  $t'$  (with  $t' > t$ ). Therefore, the returning part of a given trajectory with transverse expansion overlaps with the trajectory without transverse expansion, and the main effect of transverse expansion is on the turning point of the trajectory.

## F. QGP lifetime

We can calculate the time when the matter enters the parton phase ( $t_{\text{start}}$ ), the time when it exits the parton phase ( $t_{\text{end}}$ ), and the QGP lifetime as  $t_{\text{QGP}} = t_{\text{end}} - t_{\text{start}}$ .

Specifically, we calculate the first and last times when a  $T - \mu_B$  trajectory intersects the FRG crossover curve [35]. For very low collision energies, the trajectory does not intersect the FRG crossover curve, so we calculate  $t_{\text{start}}$  and  $t_{\text{end}}$  by finding when the trajectory intersects the line of constant energy density  $\epsilon = 0.51$  GeV/fm<sup>3</sup> shown in Fig. 3. From the results shown in Fig. 10, we see that  $t_{\text{start}}$  at a given energy is larger for a larger  $\tau_F$  as expected, and  $t_{\text{start}}$  is significantly larger at lower energies mostly due to the longer crossing time  $d_t$ . From the results without transverse expansion (dashed curves), we see that the QGP lifetime is shorter for a larger  $\tau_F$ , since  $t_{\text{end}}$  (and the late-time trajectory) is almost independent of  $\tau_F$  without transverse expansion. In addition, the QGP lifetimes from the lattice EoS are much larger than those from the quantum or Boltzmann EoS, mainly because the late-time temperatures from the lattice EoS are significantly higher as shown in Fig. 2.

When transverse expansion is considered, we see in Fig. 10 that the QGP lifetime becomes significantly shorter, especially at high energies. Note that the area between the  $t_T^{\text{norm}} = 1$  and 6 fm/c curves at each given  $\tau_F$  is shaded to show the range of transverse expansion effect, where a larger  $t_T^{\text{norm}}$  value makes the transverse flow development slower and consequently increases the QGP lifetime. The  $t_{\text{start}}$  values (curves with triangles) are essentially unaffected by the transverse expansion, because the transverse expansion takes some time to develop. However, the transverse expansion leads to lower densities at late times and thus decreases  $t_{\text{end}}$  and the QGP lifetime. For example, at  $\sqrt{s_{\text{NN}}} = 200$  GeV the QGP lifetime from the lattice EoS is  $t_{\text{QGP}} \sim 7$  fm/c with transverse expansion but  $\sim 16$  fm/c without. Therefore, the transverse expansion has a large effect on the QGP lifetime at all energies, although it has a little effect on the collision trajectory including its distance to the CEP at energies above  $\sim 7.7$  GeV. We also see that  $t_{\text{QGP}}$  is not always larger for a smaller  $\tau_F$  (more obvious for the lattice EoS results), unlike the case without transverse expansion. This behavior may seem counterintuitive at first, but it occurs because a smaller  $\tau_F$  leads to higher densities and consequently a faster transverse expansion, which leads to a smaller  $t_{\text{end}}$ .

We see in Fig. 10 that the QGP lifetime does not increase monotonously with the collision energy, as one naively expects. Instead,  $t_{\text{QGP}}$  may have a local maximum at low collision energies, which is between 3 and 5 GeV from the ideal gas EoS results shown in Figs. 10(a)-(b). Unfortunately, the lattice EoS results cannot reach very low energies due to the high  $\mu_B/T$  value there, although they also hint at an increase of  $t_{\text{QGP}}$  as  $\sqrt{s_{\text{NN}}}$  decreases below 11.5 GeV. Note that a numerical study with the AMPT model [17] has also observed the non-monotonous dependence of  $t_{\text{QGP}}$  on the collision energy for the Boltzmann EoS. After reaching the local maximum, the QGP lifetime decreases with the collision energy before it increases again, where the increase at high collision energies (after considering the transverse expansion)

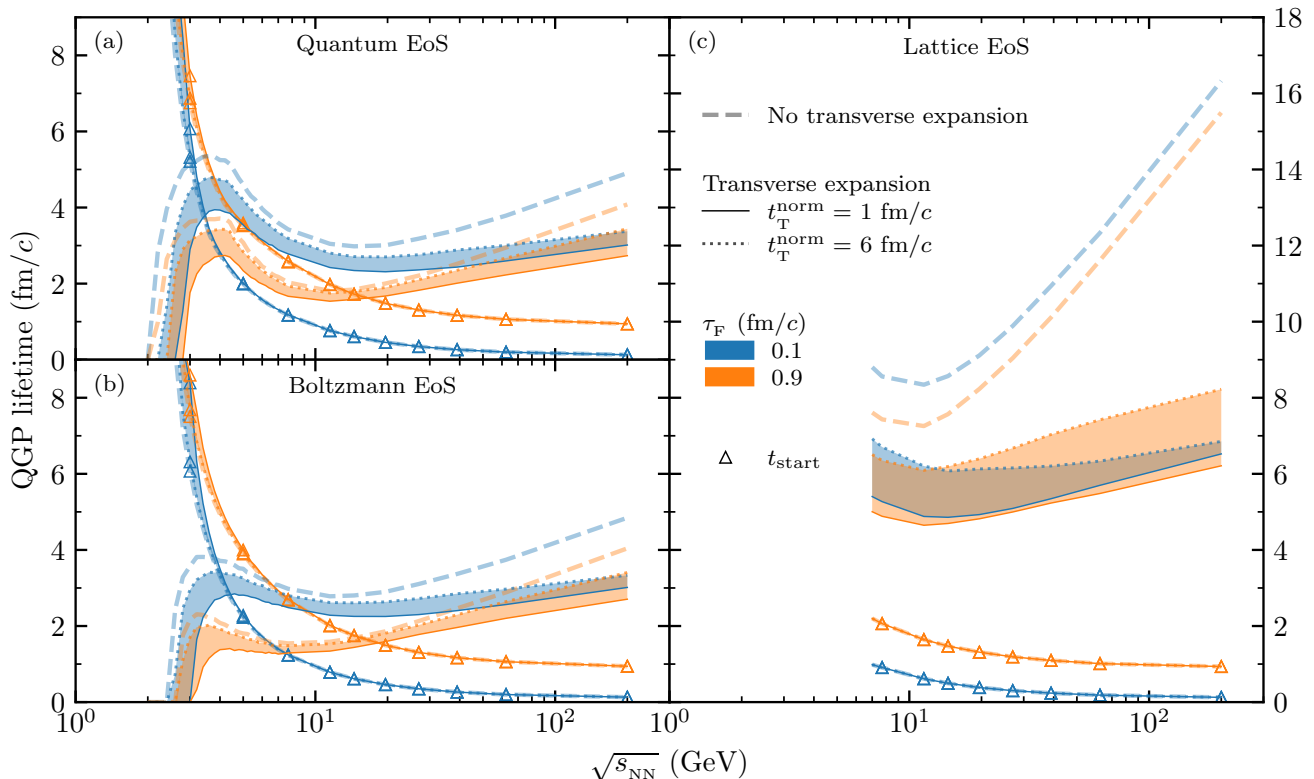


FIG. 10: The starting time (curves with triangles) and lifetime (curves without symbols) of the QGP phase in central Au+Au collisions from (a) the quantum EoS, (b) the Boltzmann EoS, and (c) the lattice EoS. Results are for  $\tau_F = 0.1$  (blue) and  $0.9$  fm/c (orange) without transverse expansion (dashed) and with transverse expansion at  $t_T^{norm} = 1$  (solid) and  $6$  fm/c (dotted).

sion) is rather slow for the lattice EoS. We also note that the STAR Collaboration recently showed that the matter produced in Au+Au collisions at  $\sqrt{s_{NN}} = 3$  GeV is likely dominated by baryonic interactions [50]. Our results in Figs. 10(a)-(b) indicate that whether the QGP could be produced in such collisions depends on the details such as the formation time, the equation of state, and the rate of transverse expansion. At  $\sqrt{s_{NN}} = 4$  GeV, on the other hand, the QGP will be formed independent of these details according to our results.

#### IV. DISCUSSIONS

In this study we use new parameterizations for  $y_B$  and  $\sigma_2$  to describe  $dN_{netB}/dy$ . We have made this change for two reasons. First, the previous parameterizations [20, 36] contain a positive power of  $\sqrt{s_{NN}}$  e.g.,  $y_B \propto (\sqrt{s_{NN}} - E_0)^{0.196} \ln^{0.392} \sqrt{s_{NN}}$ . This functional form will break down above a certain high energy because  $y_B > y_{CM}$  will eventually cause the energy in the  $dN_{netB}/dy$  term of Eq.(4) to exceed the total energy, which would be unphysical. We thus use the new forms in Eq. (7) that do not contain positive powers of  $\sqrt{s_{NN}}$ . Second, we have corrected the collision energies for the low

energy proton  $dN/dy$  data [23], from  $\sqrt{s_{NN}} = 2.4, 3.1, 3.6,$  and  $4.1$  GeV [20] to  $\sqrt{s_{NN}} = 2.65, 3.31, 3.85,$  and  $4.31$  GeV, after using the actual beam kinetic energies after correcting for the energy loss before reaching the target [23]. We also realized that the net-proton  $dN/dy$  data at  $\sqrt{s_{NN}} = 5$  GeV contain data at  $\sqrt{s_{NN}} = 4.70$  [43],  $4.86$  [24], and  $4.88$  GeV [25]. Therefore, we now combine the data at  $4.86$  GeV and  $4.88$  GeV into one data set at  $\sqrt{s_{NN}} = 4.87$  GeV. In addition, we now include the net-proton data at  $\sqrt{s_{NN}} = 8.77$  [26] and  $62.4$  GeV [28].

In Fig. 11(a), we show the updated individual fit values for  $y_B$  and  $\sigma_2$  in comparison with the old [20] and new parameterizations. At  $\sqrt{s_{NN}} < 4$  GeV, the new parameterizations for  $y_B$  and  $\sigma_2$  match the individual fit values quite well. On the other hand, the individual fit values at  $\sqrt{s_{NN}} > 4$  GeV for  $y_B$  or  $\sigma_2$  are such that it seems impossible to fit them well with a smooth function; Instead, our parameterization provides a smooth fit that is overall relatively close to most individual fit values. For example, the new parameterization overestimates the individual  $y_B$  values at  $\sqrt{s_{NN}} = 8.8$  and  $17.3$  GeV, which leads to an underestimate of  $dN_{netB}/dy(0)$ ; this is the reason why the trajectories around these energies intersect the FRG crossover curve at lower  $\mu_B$  than the RHIC chemical freezeout data as shown in Fig. 8. In

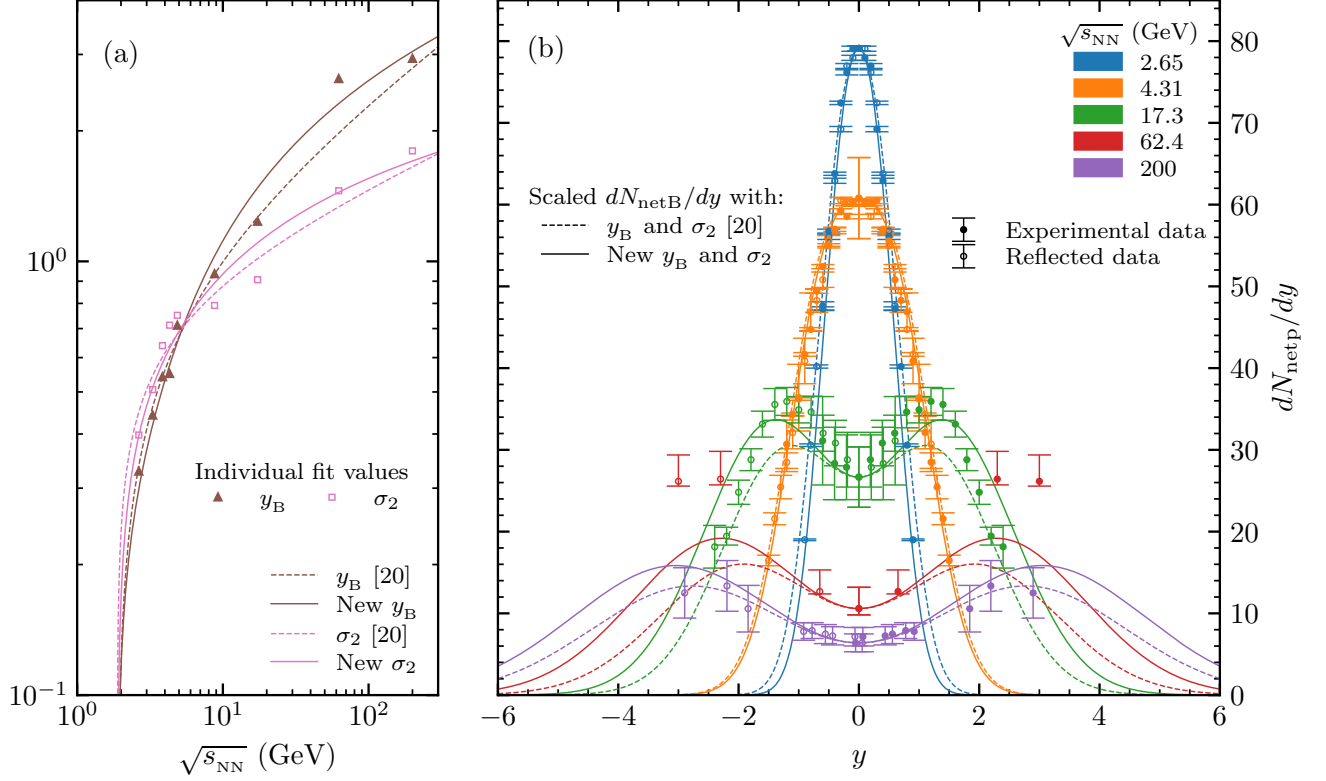


FIG. 11: (a) Individual fit values of  $y_B$  (triangles) and  $\sigma_2$  (squares) together with their previous parameterizations [20] (dashed) and new parameterizations in Eq. (7) (solid). (b) the experimental  $dN_{\text{netp}}/dy$  data (filled circles) and the values reflected across mid-rapidity (open-circles) together with scaled  $dN_{\text{netB}}/dy$  at  $\sqrt{s_{\text{NN}}} = 2.65, 4.31, 17.3, 62.4,$  and  $200$  GeV using either the parameterizations from Ref. [20] (dashed) or the new parameterizations from Eq.(7) (solid).

Fig. 11(b), we compare the  $dN_{\text{netB}}/dy$  shape from both old and new parameterizations with the net-proton data at several energies. We note that the  $dN_{\text{netB}}/dy$  shape is more sensitive to the  $y_B$  parameter than  $\sigma_2$ . We see that both parameterizations fit well the shape of the data at 2.65 and 4.31 GeV. At  $\sqrt{s_{\text{NN}}} = 17.3$  GeV, however, the new parameterization peaks at a higher rapidity than the data, which is consistent with its overestimate of the individual  $y_B$  fit value as shown in Fig. 11(a). At 62.4 GeV the new parameterization has a relatively lower peak  $dN/dy$  value than the data, consistent with its underestimate of the corresponding individual  $y_B$  fit value.

For the ideal gas equations of state, so far we have only considered a QGP consisting of massless quarks and gluons. A more realistic approach would be to consider a massive  $s$ -quark, since  $m_s = 95 \text{ MeV}/c^2$  [51] is not negligible compared to the system's temperature scale. We have not found an analytical solution for the total energy density of massive  $s$  and  $\bar{s}$  with the quantum EoS; therefore, we create an interpolating function of temperature:

$$\epsilon_s + \epsilon_{\bar{s}} = \frac{6}{\pi^2} \int_0^\infty \frac{p^2 \sqrt{p^2 + m_s^2} dp}{e^{\sqrt{p^2 + m_s^2}/T} + 1} = \epsilon_{s+\bar{s}}(T). \quad (42)$$

Note that we have used the relation  $\mu_s = 0$ , which results from the strangeness neutrality in our semi-analytical model. Considering the finite  $s$ -quark mass, we obtain the following energy density:

$$\begin{aligned} \epsilon = & \frac{37\pi^2}{30} T^4 + 3 \frac{(\mu_B - 2\mu_s)^2 + \mu_s^2}{2} T^2 \\ & + 3 \frac{(\mu_B - 2\mu_s)^4 + \mu_s^4}{4\pi^2} + \epsilon_{s+\bar{s}}(T). \end{aligned} \quad (43)$$

The equations for  $n_B$  and  $n_Q$  are unchanged from Eqs.(17) and (18), i.e., only the  $\epsilon$  equation changes when considering  $m_s \neq 0$ . We numerically solve these equations using enough  $T$  sampling points for  $\epsilon_{s+\bar{s}}(T)$  to ensure accuracy. We have compared the resulting  $T - \mu_B$  trajectories to those for  $m_s = 0 \text{ MeV}/c^2$  and have observed essentially no difference in the  $T - \mu_B$  results including the QGP lifetime when considering a non-zero  $s$ -quark mass. Note that a similar lack of effect from finite quark masses have also been seen in numerical studies from the AMPT model [17].

We have observed  $\mu_Q \simeq 0$  in the full solutions for both quantum and Boltzmann ideal gas equations of state, as shown in Figs. 2 and 5. As a result, the partial-1 solution assumes  $\mu_Q = 0$  and then gives almost the

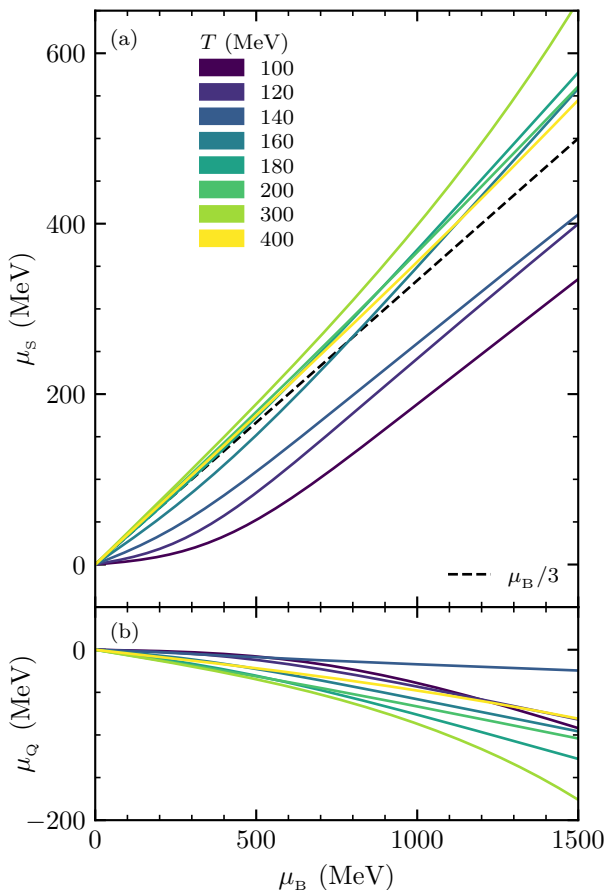


FIG. 12: Chemical potential (a)  $\mu_s$  and (b)  $\mu_Q$  versus  $\mu_B$  at various temperatures for the lattice EoS under the condition  $n_Q = n_B Z/A$  (for Au) and  $n_s = 0$ . The dashed line represents  $\mu_s = \mu_B/3$ .

same  $T - \mu_B$  trajectories as the full solution. Therefore, a natural question is why  $\mu_Q$  is so small. To answer this question, we first observe that our semi-analytical model [20] gives  $n_s(t) = 0$ . In addition, our model predicts  $n_Q(t) = n_B(t)/2$  if  $Z = A/2$  for the colliding nuclei. One can verify that,  $n_s = 0$  and  $n_Q = n_B/2$  lead to  $\mu_Q = 0$  for both statistics in the ideal gas EoS. Therefore,  $\mu_Q \simeq 0$  is a consequence of the fact that most nuclei have  $Z \sim A/2$ . Note that recent results from the AMPT model [30] also show  $\mu_Q \approx 0$  [17], although the AMPT model does not assume the  $s$ - $\bar{s}$  symmetry for the initial production and thus does not give  $n_s(t) = 0$  exactly. We also note that the  $\mu_Q$  values extracted with the lattice EoS are sometimes significantly larger than those from the full solution of the ideal gas EoS with either statistics.

We examine in Fig. 12 the strangeness neutrality in the lattice EoS by plotting the  $\mu_B$  dependence of  $\mu_s$  and  $\mu_Q$  for various temperatures. Note that the lattice EoS results are obtained under the condition of Eq.(34) using the  $Z$  and  $A$  value for the gold nucleus. We see  $\mu_s \simeq \mu_B/3$

for temperatures higher than  $T \gtrsim 160$  MeV. For lower  $T$ , however, this approximation does not describe the lattice results, which are expected to be trustworthy at least at low  $\mu_B$  [33]. These features are very similar to the FRG results [52]. The results from the FRG method also show a strict ordering of  $\mu_s(\mu_B)$  with  $T$ , where the  $\mu_s$  result at higher  $T$  gets closer to the  $\mu_s = \mu_B/3$  line. The lattice EoS results in Fig. 12 show a similar ordering of  $\mu_s$  below  $T \sim 180$  MeV but no clear ordering at higher temperatures in either  $\mu_s$  or  $\mu_Q$ . In addition, in the region  $\mu_B/T < 2.5$  we observe that  $\mu_Q$  is small with a magnitude not larger than  $\sim 60$  MeV. Overall, the partial-1 assumptions of  $\mu_Q = 0$  and  $\mu_s = \mu_B/3$  work less well for the lattice EoS than for the ideal gas EoS. We find that for the lattice EoS the trajectories calculated with these assumptions can have  $T$  and  $\mu_B$  values different by up to  $\sim 2\%$  and  $\sim 16\%$ , respectively; interestingly, the calculated QGP lifetime is not much different.

Since our model is semi-analytical, it is a convenient tool for calculating the trajectories of nuclear collisions in the QCD phase diagram, either in the conventional  $T - \mu_B$  plane or the more general  $T - \mu_B - \mu_Q - \mu_s$  four-dimensional space. We have extended the web interface [53] that performs the semi-analytical calculation of  $\epsilon(t)$  for central A+A collisions depending on the user input for the colliding system, energy, and the proper formation time  $\tau_F$ . It [53] now performs the semi-analytical calculations of  $\epsilon(t)$ ,  $n(t)$ ,  $T(t)$ , and  $\mu(t)$  for either the quantum or Boltzmann ideal gas equations of state and also plots the  $T - \mu_B$  trajectory. We plan to further extend the web interface to include the lattice EoS and transverse expansion.

## V. CONCLUSIONS

We have extended a semi-analytical model, which considers the finite nuclear thickness, to calculate the energy density  $\epsilon(t)$ , net-baryon density  $n_B(t)$ , net-charge density  $n_Q(t)$ , and net-strangeness density  $n_s(t)$  at mid-spacetime-rapidity averaged over the full transverse area of central Au+Au collisions. We then extract the temperature  $T(t)$ , baryon chemical potential  $\mu_B(t)$ , electric charge chemical potential  $\mu_Q(t)$ , and strangeness chemical potential  $\mu_s(t)$  of the parton system assuming the formation of an equilibrated QGP. We use an ideal gas equation of state of either quantum or Boltzmann statistics or a lattice QCD-based equation of state. We find that the trajectory in the  $T - \mu_B$  plane significantly depends on the EoS; for example, the critical end point from the FRG method is located close to the  $\sqrt{s_{NN}} \sim 4$  GeV trajectory when using the quantum ideal gas EoS but the  $\sqrt{s_{NN}} \sim 3$  GeV trajectory when using the Boltzmann ideal gas EoS.

By calculating the trajectory endpoint as a function of collision energy, we obtain the  $T - \mu_B$  area that the mid-pseudorapidity region of central Au+Au collisions can cover. We find that the accessible area in the phase dia-



gram depends strongly on the parton formation time  $\tau_F$ , once the collision energy is higher than several GeV. On the other hand, the critical end point from the FRG calculation is well within the accessible area, even for a large formation time of  $\tau_F = 0.9$  fm/ $c$ . We also observe that the trajectory using the Bjorken energy density method is significantly different at low collision energies, which further demonstrates the importance of the finite nuclear thickness at low energies such as the BES energies. In addition, we find that the transverse expansion has a small effect on the collision trajectory but a large effect on the QGP lifetime, while the QGP lifetime for the lattice EoS is much larger than those for the ideal gas EoS. We further observe an unexpected increase in the QGP lifetime as the collision energy decreases below  $\sqrt{s_{NN}} \sim 11.5$  GeV. Overall, our semi-analytical model provides a useful tool for exploring the trajectories of nuclear collisions in the QCD phase diagram in the  $T - \mu_B$  plane or in the more general  $T - \mu_B - \mu_Q - \mu_S$  space.

### Acknowledgments

This work has been supported by the National Science Foundation under Grant No. 2012947. We thank Wei-jie Fu, Guo-Liang Ma, Han-Sheng Wang, Claudia Ratti, and Christina Markert for helpful discussions. We also thank Wei-jie Fu for providing the crossover and CEP results from FRG calculations.

### Appendix: Thermodynamics relations between $\epsilon$ , $n$ and $T$ , $\mu$ for a QGP with ideal gas equations of state

We consider a quark-gluon plasma composed of gluons  $g$  and three quark flavors, similar to a previous study [17]. The total energy, net-baryon, net-electric charge, and net-strangeness densities are then given by

$$\begin{aligned} \epsilon &= \epsilon_g + \sum_q (\epsilon_q + \epsilon_{\bar{q}}), & n_B &= \sum_q B_q (n_q - n_{\bar{q}}), \\ n_Q &= \sum_q Q_q (n_q - n_{\bar{q}}), & n_S &= \sum_q S_q (n_q - n_{\bar{q}}), \end{aligned} \quad (\text{A.1})$$

where  $B_q$ ,  $Q_q$ , and  $S_q$  are the quark baryon, electric charge, and strangeness numbers, respectively, for quark

flavor  $q$  with  $q = u, d, \text{ or } s$ . For parton flavor  $i$ , the energy and number densities are given by

$$\begin{aligned} \epsilon_i &= \frac{1}{2\pi^2} \int_0^\infty dp p^2 \sqrt{p^2 + m_i^2} f_i(p), \\ n_i &= \frac{1}{2\pi^2} \int_0^\infty dp p^2 f_i(p), \end{aligned} \quad (\text{A.2})$$

respectively, where  $m_i$  represents the parton mass, and  $f_i(p)$  is given by

$$f_i(p) = d_i \left[ \exp\left(\frac{\sqrt{p^2 + m_i^2} - \mu_i}{T}\right) + K \right]^{-1}. \quad (\text{A.3})$$

In the above, the degeneracy factor  $d_i$  is 16 for gluons and 6 for quarks,  $\mu_i$  is the parton chemical potential,  $T$  is the temperature,  $K = 1$  for Fermi-Dirac statistics,  $-1$  for Bose-Einstein statistics, and 0 for Boltzmann statistics. The chemical potential of parton flavor  $i$  is  $\mu_i = B_i \mu_B + Q_i \mu_Q + S_i \mu_S$ , where  $\mu_B$ ,  $\mu_Q$ , and  $\mu_S$  are the baryon, electric charge, and strangeness chemical potentials, respectively.

### 1. Massless QGP with quantum statistics

For a massless quark-gluon plasma with quantum statistics, we take  $\mu_g = 0$ ,  $\mu_q + \mu_{\bar{q}} = 0$  and then obtain

$$\begin{aligned} \epsilon_q + \epsilon_{\bar{q}} &= -\frac{18T^4}{\pi^2} \left[ Li_4\left(-e^{-\mu_q/T}\right) + Li_4\left(-e^{\mu_q/T}\right) \right] \\ &= \frac{7\pi^2}{20} T^4 + \frac{3\mu_q^2}{2} T^2 + \frac{3\mu_q^4}{4\pi^2}, \\ n_q - n_{\bar{q}} &= \frac{6T^3}{\pi^2} \left[ Li_3\left(-e^{-\mu_q/T}\right) - Li_3\left(-e^{\mu_q/T}\right) \right] \\ &= \mu_q T^2 + \frac{\mu_q^3}{\pi^2}, \end{aligned} \quad (\text{A.4})$$

where  $Li_n(z)$  is the polylogarithm function of order  $n$ . Therefore, we obtain the following:

$$\epsilon = \frac{19\pi^2}{12}T^4 + \frac{(\mu_B + 2\mu_Q)^2 + (\mu_B - \mu_Q)^2 + (\mu_B - \mu_Q - 3\mu_S)^2}{6}T^2 + \frac{(\mu_B + 2\mu_Q)^4 + (\mu_B - \mu_Q)^4 + (\mu_B - \mu_Q - 3\mu_S)^4}{108\pi^2}, \quad (\text{A.5})$$

$$n_B = \frac{\mu_B - \mu_S}{3}T^2 + \frac{(\mu_B + 2\mu_Q)^3 + (\mu_B - \mu_Q)^3 + (\mu_B - \mu_Q - 3\mu_S)^3}{81\pi^2}, \quad (\text{A.6})$$

$$n_Q = \frac{2\mu_Q + \mu_S}{3}T^2 + \frac{2(\mu_B + 2\mu_Q)^3 - (\mu_B - \mu_Q)^3 - (\mu_B - \mu_Q - 3\mu_S)^3}{81\pi^2}, \quad (\text{A.7})$$

$$n_S = -\frac{\mu_B - \mu_Q - 3\mu_S}{3}T^2 - \frac{(\mu_B - \mu_Q - 3\mu_S)^3}{27\pi^2}. \quad (\text{A.8})$$

## 2. Massless QGP with Boltzmann statistics

Using the Maxwell-Boltzmann statistics to describe the thermodynamics of the quark-gluon plasma, for

massless partons we obtain the following equations that are simpler than those for finite quark masses [17]:

$$\epsilon = \frac{12}{\pi^2}T^4 \left[ 4 + 3 \cosh\left(\frac{\mu_B + 2\mu_Q}{3T}\right) + 3 \cosh\left(\frac{\mu_B - \mu_Q}{3T}\right) + 3 \cosh\left(\frac{\mu_B - \mu_Q - 3\mu_S}{3T}\right) \right], \quad (\text{A.9})$$

$$n_B = \frac{4}{\pi^2}T^3 \left[ \sinh\left(\frac{\mu_B + 2\mu_Q}{3T}\right) + \sinh\left(\frac{\mu_B - \mu_Q}{3T}\right) + \sinh\left(\frac{\mu_B - \mu_Q - 3\mu_S}{3T}\right) \right], \quad (\text{A.10})$$

$$n_Q = \frac{4}{\pi^2}T^3 \left[ 2 \sinh\left(\frac{\mu_B + 2\mu_Q}{3T}\right) - \sinh\left(\frac{\mu_B - \mu_Q}{3T}\right) - \sinh\left(\frac{\mu_B - \mu_Q - 3\mu_S}{3T}\right) \right], \quad (\text{A.11})$$

$$n_S = -\frac{12}{\pi^2}T^3 \sinh\left(\frac{\mu_B - \mu_Q - 3\mu_S}{3T}\right). \quad (\text{A.12})$$

- 
- [1] P. Jacobs and X.-N. Wang, *Prog. Part. Nucl. Phys.* **54**, 443 (2005).  
[2] B. Tomasik and U. A. Wiedemann, *in Quark Gluon Plasma 3*, edited by R. C. Hwa and X. N. Wang (WORLD SCIENTIFIC, Singapore, 2004).  
[3] J. Adams et al. (STAR), *Nucl. Phys. A* **757**, 102 (2005).  
[4] Y. Aoki, G. Endrodi, Z. Fodor, S. D. Katz, and K. K. Szabo, *Nature* **443**, 675 (2006).  
[5] R. Bellwied, S. Borsanyi, Z. Fodor, J. Günther, S. D. Katz, C. Ratti, and K. K. Szabo, *Phys. Lett. B* **751**, 559 (2015).  
[6] A. Bazavov et al. (HotQCD), *Phys. Lett. B* **795**, 15 (2019).  
[7] R. V. Gavai and S. Gupta, *Phys. Rev. D* **68**, 034506 (2003).  
[8] M. A. Stephanov, *Prog. Theor. Phys. Suppl.* **153**, 139 (2004).  
[9] M. M. Aggarwal et al. (STAR), *Phys. Rev. Lett.* **105**, 022302 (2010).  
[10] J. Adam et al. (STAR), *Phys. Rev. Lett.* **126**, 092301 (2021).  
[11] L. Adamczyk et al. (STAR), *Phys. Rev. Lett.* **112**, 032302 (2014).  
[12] V. Koch, A. Majumder, and J. Randrup, *Phys. Rev. Lett.* **95**, 182301 (2005).  
[13] X. Luo and N. Xu, *Nucl. Sci. Tech.* **28**, 112 (2017).  
[14] B. Zhang, L.-W. Chen, and C. M. Ko, *J. Phys. G* **35**, 065103 (2008).  
[15] Z.-W. Lin, *Phys. Rev. C* **90**, 014904 (2014).  
[16] C. Shen and L. Yan, *Nucl. Sci. Tech.* **31**, 122 (2020).  
[17] H.-S. Wang, G.-L. Ma, Z.-W. Lin, and W.-j. Fu, *Phys. Rev. C* **105**, 034912 (2022).  
[18] J. D. Bjorken, *Phys. Rev. D* **27**, 140 (1983).  
[19] Z.-W. Lin, *Phys. Rev. C* **98**, 034908 (2018).  
[20] T. Mendenhall and Z.-W. Lin, *Phys. Rev. C* **103**, 024907 (2021).  
[21] K. Adcox et al. (PHENIX), *Nucl. Phys. A* **757**, 184 (2005).

- [22] S. S. Adler et al. (PHENIX), *Phys. Rev. C* **71**, 034908 (2005).
- [23] J. L. Klay et al. (E895), *Phys. Rev. Lett.* **88**, 102301 (2002).
- [24] L. Ahle et al. (E802), *Phys. Rev. C* **60**, 064901 (1999).
- [25] B. B. Back et al. (E917), *Phys. Rev. Lett.* **86**, 1970 (2001).
- [26] T. Anticic et al. (NA49), *Phys. Rev. C* **83**, 014901 (2011).
- [27] H. Appelshauser et al. (NA49), *Phys. Rev. Lett.* **82**, 2471 (1999).
- [28] I. C. Arsene et al. (BRAHMS), *Phys. Lett. B* **677**, 267 (2009).
- [29] I. G. Bearden et al. (BRAHMS), *Phys. Rev. Lett.* **93**, 102301 (2004).
- [30] Z.-W. Lin, C. M. Ko, B.-A. Li, B. Zhang, and S. Pal, *Phys. Rev. C* **72**, 064901 (2005).
- [31] A. Monnai, B. Schenke, and C. Shen, *Int. J. Mod. Phys. A* **36**, 2130007 (2021).
- [32] S. Borsanyi, Z. Fodor, J. N. Guenther, S. K. Katz, K. K. Szabo, A. Pasztor, I. Portillo, and C. Ratti, *JHEP* **10**, 205 (2018).
- [33] J. Noronha-Hostler, P. Parotto, C. Ratti, and J. M. Stafford, *Phys. Rev. C* **100**, 064910 (2019).
- [34] P. Huovinen and P. Petreczky, *Phys. Lett. B* **777**, 125 (2018).
- [35] W.-j. Fu, J. M. Pawlowski, and F. Rennecke, *Phys. Rev. D* **101**, 054032 (2020).
- [36] Z.-W. Lin and T. Mendenhall, *Rev. Mex. Fis. Suppl.* **3**, 040920 (2022).
- [37] L. Adamczyk et al. (STAR), *Phys. Rev. C* **96**, 044904 (2017).
- [38] B. I. Abelev et al. (STAR), *Phys. Rev. C* **79**, 034909 (2009).
- [39] B. Abelev et al. (ALICE), *Phys. Rev. C* **88**, 044910 (2013).
- [40] Y. Akiba et al. (E802), *Nucl. Phys. A* **610**, 139C (1996).
- [41] L. Ahle et al. (E-802), *Phys. Rev. C* **57**, R466 (1998).
- [42] L. Ahle et al. (E866, E917), *Phys. Lett. B* **476**, 1 (2000).
- [43] J. Barrette et al. (E877), *Phys. Rev. C* **62**, 024901 (2000).
- [44] L. Ahle et al. (E-802, E-866), *Phys. Rev. C* **60**, 044904 (1999).
- [45] L. Ahle et al. (E866, E917), *Phys. Lett. B* **490**, 53 (2000).
- [46] C. Alt et al. (NA49), *Phys. Rev. C* **77**, 024903 (2008).
- [47] C. Alt et al. (NA49), *Phys. Rev. C* **73**, 044910 (2006).
- [48] T. Anticic et al. (NA49), *Phys. Rev. C* **69**, 024902 (2004).
- [49] S. V. Afanasiev et al. (NA49), *Phys. Rev. C* **66**, 054902 (2002).
- [50] M. S. Abdallah et al. (STAR), *Phys. Lett. B* **827**, 137003 (2022).
- [51] P. A. Zyla et al. (Particle Data Group), *Prog. Theor. Exp. Phys.* **2020**, 083C01 (2020).
- [52] W.-j. Fu, J. M. Pawlowski, and F. Rennecke, *Phys. Rev. D* **100**, 111501 (2019).
- [53] A web interface that performs the semi-analytical calculation of the collision trajectory of central A+A collisions for selected equations of state is available at <https://myweb.ecu.edu/linz/densities/> (2022).